Green energy storage materials: Nanostructured TiO_2 and Sn-based anodes for lithium-ion batteries

Da Deng,[a] Min Gyu Kim,[b] Jim Yang Lee*[a] and Jaephil Cho*[c]

Received 5th January 2009, Accepted 3rd April 2009
First published as an Advance Article on the web 21st April 2009
DOI: 10.1039/b823474d

It is expected that the market dominance of lithium-ion batteries will continue for at least another decade as there are currently no competing alternatives with the versatility of lithium-ion batteries for powering mobile and portable devices; and for buffering the fluctuating supply of intermittent energy sources such as wind and solar. While the pursuit of higher energy density and higher power density materials constitute the bulk of current interest, there is increasing interest in durable active battery materials that can be produced with minimum environmental impact. It is with these considerations that TiO_2- and Sn-based anode materials are most interesting candidates for fulfilling future green energy storage materials. This review will focus on the recent developments of nanostructured TiO_2 and Sn-based anode materials, including rutile, anatase, TiO_2 (B), and coated TiO_2, and pristine SnO_2, and SnO_2/C, Sn(M)/C composites.

Introduction

Lithium-ion batteries (LIBs) are considered the most promising energy storage technologies for mobile electronics, electric vehicles and renewable energy systems operating on intermittent energy sources such as wind and solar.[1] Usually LIBs are connected in series or in parallel to deliver the user specified electrical characteristics. The active cathode and anode materials in a typical LIB are $LiCoO_2$ and graphite respectively (Fig. 1); electrically insulated by a porous polypropylene membrane separator and an intervening electrolyte of $LiPF_6$ in a mixture of organic solvents (*e.g.* ethylene carbonate and diethyl carbonate). During discharging, the electrochemical potential difference between the anode and cathode drives the Li^+ ions to move from anode to cathode internally through the electrolyte. The reverse process occurs during charging.[2,3] The reversibility of the charge and discharge reactions at the electrodes determines the reversibility of the battery. The three most important performance indicators for a LIB are capacity, cyclability and rate capability, which are strongly dependent on the properties of the active electrode materials. For emerging applications, however, fundamental improvements are needed with regard to power, safety, cycle life, and cost. Research into low price and high efficiency energy storage materials have been recently intensified, and among various candidates, TiO_2 and SnO_2 materials have been intensively investigated due to their versatile and easy modification of nanostructures.

Downsizing from conventional bulk state to nanoscale dimensions has been widely used as the means to increase the energy storage capacity of TiO_2.[4] In 1998, Kasuga *et al.* first reported a simple template-free method to synthesize TiO_2 nanotubes from amorphous TiO_2 and 10 M NaOH in a hydrothermal reactor at 110 150 °C, followed by washing with 0.1 M HCl.[5,6] TiO_2 is a typical Li-ion intercalation compound with a volume change < 4% in the reaction: $TiO_2 + xLi^+ xe^- \leftrightarrow Li_xTiO_2$ ($0 \leq x \leq 1$). It is most noted for its ease of fabrication into various particle morphologies such as nanotubes, nanowires, and nanoparticles.[7–12] The negligible lattice changes of TiO_2-based structures upon Li-ion intercalation and de-intercalation are responsible for the enhanced structural stability and longer cycle life. One drawback, however, is the poor lithium and electronic conductivity of the bulk state and low specific capacity. One strategy to address these issues is the use of

[a]*Department of Chemical & Biomolecular Engineering, Faculty of Engineering, National University of Singapore, 10 Kent Ridge Crescent, Singapore 119260. E-mail: cheleejy@nus.edu.sg*
[b]*Beamline Research Division, Pohang Accelerator Laboratory, Pohang, Korea 790-784*
[c]*School of Energy Engineering, Ulsan National Institute of Science & Technology, Ulsan, Korea 689-805. E-mail: jpcho@unist.ac.kr*

Broader context

It is expected that the market dominance of lithium-ion batteries will remain for at least another decade as there are currently no competing alternatives with the versatility of lithium ion batteries for powering mobile and portable devices; and for buffering the fluctuating supply of intermittent energy sources such as wind and solar. While the pursuit of higher energy density and higher power density materials constitute the bulk of current interest, there is increasing interest in durable active battery materials that can be produced with minimum environmental impact. It is with these considerations that TiO_2- and Sn-based anode materials are most interesting candidates for fulfilling future green energy storage materials. This review will focus on the recent developments of nanostructured TiO_2 and Sn-based anode materials.

 This journal is © The Royal Society of Chemistry 2009

Samsung Ex. 1040, Page 1 of 20
Samsung Electronics Co., Ltd., et al. v. Molecular Rebar Design, LLC
IPR2025-00356

nanostructured TiO_2 materials. The large surface area of nanostructured TiO_2 materials increases the electrolyte/electrode contact area, which leads to the decrease of the current density per unit surface area and an increase in the charge/discharge rate. Moreover, the nanostructure provides a shorter path for Li^+ transport, permitting the battery to use materials with lower ionic conductivity. The high surface area, on the other hand, incurs more side reactions with the electrolyte, and the thickness of the solid electrolyte interface (SEI) layer may be larger than in the case of bulk TiO_2 impeding electron and Li ion transport in and out of the structure. In the case of nanoporous TiO_2, due to the increased volume fraction of the pores, volumetric energy density also decreases compared to bulk TiO_2.

On the other hand, considering the fact that the graphite-based anode is now approaching its theoretical limit of 372 mAh g^{-1} (based on LiC_6 stoichiometry), there is a need for the next generation of LIBs to find a higher capacity substitute for the graphite anode.[13–16] In 1997 Fujifilm announced an amorphous tin-based composite oxide anode (TCO) for LIBs.[17,18] The design made use of Li Sn alloying and de-alloying reactions for Li^+ storage where the idealized stoichiometry of $Li_{4.4}Sn$ could deliver a capacity more than double that of graphite (993 mAh g^{-1}). Although Fujifilm subsequently failed to commercialize the TCO anode because of poor cycling performance, it has started worldwide interest in anode materials based on metal oxides.[15,16,19] Very recently Sony announced a new generation of LIBs with the trade name of Nexelion, which is based on a carbon tin transition metal composite (*e.g.* Sn Co C). Although the exact composition of the Li storage compound is not disclosed, this successful effort has rekindled another wave of interest in Li storage in tin-based host materials.[20–23]

Da Deng received a BEng degree in Environmental Engineering from National University of Singapore (NUS). He is currently a PhD candidate (with Prof. J. Y. Lee) in Chemical and Biomolecular Engineering at NUS. His PhD research project focuses on the design, synthesis and characterization of materials for Li-ion batteries and for self-cleaning applications.

Jim Yang Lee is Professor of Chemical and Bimolecular Engineering at NUS. He is a Senior Fellow of the Energy Studies Institute and holds an adjunct appointment at the Institute of Materials Research and Engineering. His research interests include materials and processes for batteries and fuel cells, and the green synthesis of nanostructured materials.

Min Gyu Kim is a senior researcher at the Pohang Accelerator Laboratory (PAL), Korea. He received a PhD in Chemistry from Yonsei University (Korea) in 2000. After completing a post-doctoral fellowship at the Department of Chemical Engineering, Pohang University of Science and Technology (POSTECH) (Korea) he joined the beamline research division of PAL in 2002. He is currently in charge of a BL7C1 (XAFS-II) beamline dedicated to X-ray Absorption Fine Structure and beamline construction of BL10A (HF-XAFS) with a Wiggler insertion device. His research interests focus on solid state chemistry combined with synchrotron radiation XAFS and X-ray scattering, covering the synthesis and characterization of low-dimensional materials for energy storage conversion materials, intercalation and organic inorganic hybrid materials.

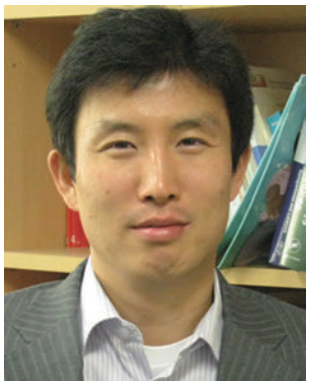

Jaephil Cho is Professor of Energy Engineering at Ulsan National Institute of Science & Technology, Korea. He received a MS and PhD in Ceramic Engineering from Iowa State University (USA) in 1993 and 1995, respectively, and a BS in Materials Engineering from Kyungpook National University (Korea) in 1990. In 1995, he joined the School of Materials Science and Engineering at Georgia Institute of Technology (USA) as a post-doctoral fellow, studying Li-ion conducting glass and polymer composite solid electrolytes and combustion reactions of cathode materials. He moved to R & D at Samsung SDI Co. Ltd as a Senior Researcher in 1996, and worked on the development of Li-ion battery cathode materials until August, 2002. From September, 2002 to 2007 and 2008, he was Professor of Applied Chemistry at Kumoh National Institute of Technology and Hanyang University (Korea). His current research is focused mainly on nanomaterials for energy conversion and storage, nanoscale coating, and safety enhancement of Li-ion batteries.

Samsung Ex. 1040, Page 2 of 20
Samsung Electronics Co., Ltd., et al. v. Molecular Rebar Design, LLC
IPR2025-00356

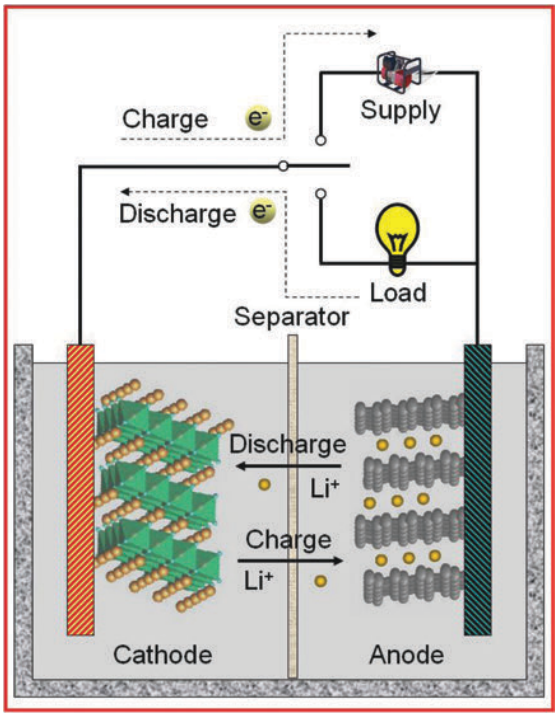

Fig. 1 The components of a typical lithium-ion battery and the electrochemical processes in charging and discharging. The typical cathode and anode materials are $LiCoO_2$ and graphite respectively.

The most-studied tin-based Li storage compound is tin oxide. In its first cycle of use, SnO_2 is irreversibly converted to tin according to eqn (1) below. Subsequently, the *in-situ* formed tin phase could store and release Li ions according to the Li Sn alloying and de-alloying reactions shown by eqn (2) below:

$$SnO_2 + 4Li^+ + 4e^- \rightarrow Sn + 2Li_2O \quad (1)$$

$$Sn + xLi^+ + xe^{-1} \leftrightarrow Li_xSn \ (0 \leq x \leq 4.4) \quad (2)$$

It is now known that the poor cycling performance of tin is caused by large specific volume changes (up to 300%) in charge and discharge reactions leading to the mechanical disintegration of the anode and loss of electrical connectivity between the active materials.[24] One of the mitigating strategies to improve material stability is to reduce the active electrode material to the nanoscale.[13,14,16,19,25,26] Nanomaterials, owing to their small size, are more accommodating to compressive and tensile strains.[27] The high surface/volume ratio increases the electrode/electrolyte interface and promotes faster diffusion of Li^+ ions within the material so that a higher charging rate is possible. Furthermore, certain irreversible electrochemical reactions in the bulk state could be made more reversible at the nanoscale. Eqn (1) is a good example.[28] This could explain the higher than theoretical specific capacity that is sometimes observed in phase-pure SnO_2 nanomaterials. The main disadvantage of tin-based nanomaterials is their lower volumetric energy density.[27] On the other hand, it is known that the properties of nanomaterials are strongly structure and morphology dependent. Hence the transition from simple 0-dimensional (0-D) nanoparticles to a high-order nanostructure may offer opportunities to "tune-in" properties desirable for the intended application. However, the facile preparation of high-order nanostructured tin-based electrode materials is not a trivial exercise.

This review will focus on recent developments in TiO_2 and tin-based anode materials for the LIBs. In the case of TiO_2, we focus on the review on the electrochemical properties of three types of TiO_2, that is, rutile, anatase, and TiO_2 (B); especially their high rate performance which is significantly affected by the particle size and morphology. In addition, coating on the TiO_2 host will be discussed as a means to increase electronic conductivity of the host at higher current (C) rates. In the case of Sn-based electrodes, due to the large amount of available literature; we will limit the review to cover only new and novel synthesis methods and the preparation of intriguing nanostructures, especially the work carried out in the authors' laboratories. Consequently the discussions below are organized into the following sections: template-assisted and template-free fabrications of SnO_2 nanostructures, SnO_2/C composite nanostructures, and Sn/C and Sn M/C nanomaterials.

2. TiO_2

2.1. Rutile

Rutile TiO_2 (P42/mnm) is the most common and stable form of TiO_2 (Fig. 2). The tetragonal rutile modification consists of TiO_6 octahedra sharing edges in the *c*-direction and corners in the *ab* plane.[29] The preferential site for Li^+ insertion has been reported to be the oxygen octahedral vacancy.[30] To reach this position, Li^+ has to migrate through the tetrahedral site, which is neighbor to the octahedral site in the *ab*-plane (Fig. 2). Due to this special arrangement, Li^+ diffusion in rutile is highly anisotropic. Experimental results and simulations support that the Li^+ diffusion coefficient along the *c*-direction is approximately 10^{-6} $cm^2\ s^{-1}$, while it is only 10^{-15} $cm^2\ s^{-1}$ in the *ab*-plane, rendering Li^+ diffusion in rutile nearly one dimensional.[29,31,32] This means that Li diffusion proceeds through rapid diffusion along the *c*-axis channels. At low temperature the very slow diffusion in the *ab* planes $D_{ab} = 10^{-15}$ $cm^2\ s^{-1}$ prevents Li ions from reaching the thermodynamically favorable octahedral sites and separates Li^+ in the *c* channels.[29,31,32] The repulsive Li Li interactions in *c* together with the trapped Li-ion pairs in the *ab* planes may block the *c* channels and prevent further insertion.[33]

Generally, bulk rutile TiO_2 is reported to host only a negligible amount of Li ions except at elevated temperatures. Although it shows high Li-ion diffusion coefficient in the order of $\sim 10^{-6}$ $cm^2\ s^{-1}$, the one-dimensional character of the diffusion limits the

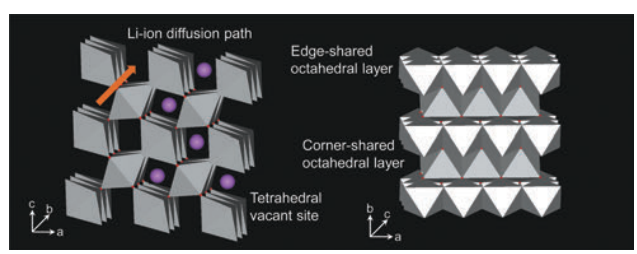

Fig. 2 Structure of rutile TiO_2.

This journal is © The Royal Society of Chemistry 2009

Samsung Ex. 1040, Page 3 of 20
Samsung Electronics Co., Ltd., et al. v. Molecular Rebar Design, LLC
IPR2025-00356

Li-ion insertion over significant 3D volumes, causing the poor performance of the bulk materials. Since full Li loading ($x = 1$) of rutile could be achieved at 120 °C,[34] Li^+ insertion into rutile is thermodynamically favorable. Yet, with the very low current density of C/300 (*i.e.*, one lithium per formula unit in 300 h) used to discharge the micrometer-sized rutile electrodes at room temperature, the capacity was reported to be very low.[35] This result suggests that the difficulty of Li insertion into micrometer-sized rutile at room temperature is due to kinetic restrictions.

Recently, it was found that nanosizing strongly increases both the capacity ($\sim Li_{0.85}TiO_2$) and the rate capability.[35] However, both bulk and nanoparticle TiO_2 show low coulombic efficiencies, and a reason for this phenomenon is reported to be related to possible formation of a new phase around $Li_{0.4}TiO_2$, and the new phase is either a hexagonal structure (R-3m) or a cubic rock salt structure (Fm-3m). Molecular dynamics simulations of the Li-ion diffusion in the rutile structure revealed that maximum (chemically) lithiated microrutile ($\sim$0.43 Li/Ti at room temperature) represents the formation of a layered morphology having a monoclinic symmetry ($P2/m$) similar to the previously suggested layered hexagonal structure.[36] Further lithiation of the nanomaterial up to Li/Ti = 0.53 resulted in a phase transition toward an intermediate phase, very similar to the original rutile phase but slightly deformed, reducing the symmetry to the monoclinic $P2/m$ space group. Upon further Li-ion insertion, up to $\sim$0.85 Li/Ti, this phase transformed toward another structure, again indexed by the monoclinic $P2/m$ space group but now similar to the layered hexagonal $R\bar{3}m$ space group previously suggested to form in rutile TiO_2 upon lithiation.[18]

The solid solution regime consisting of the coexistence of two phase region in microsized rutile is limited to $x \sim 0.07$ Li/Ti. However, in the nanomaterial, the solid solution domain can extend up to $x = 0.15$ Li/Ti (*i.e.*, further than in the micromaterial). This provides more evidence that reducing the crystallite size minimizes the miscibility gap of two-phase reactions upon lithiation, especially when lattice mismatches lead to strains between the phases, such as that recently demonstrated for anatase TiO_2 (Fig. 3).[37] On the other hand, the high specific surface area of nanocrystalline rutile provides more active sites for Li insertion and also for surface Li-ion storage. Li diffusion proceeds mainly through the *c* channels in rutile, but the thermodynamically stable positions for Li accommodation are the octahedral sites in the *ab* planes.[32] The sluggish Li diffusion in the *ab* planes thus becomes the bottleneck for further Li insertion. Consequently, Li insertion occurs mostly on a thin surface layer rather than in the bulk. In the case of the most stable (110) surface of rutile, lithium insertion is mainly a surface effect because the Li atoms do not penetrate into the bulk. Hence increasing the specific surface area will enable a more pronounced Li-ion storage capability in the particle surface areas. There are two mechanisms for active Li-ion storage: storage of Li ions in the bulk (volume) of the material through intercalation or insertion reactions; and storage of Li ions at the material surface through electric double layer effects and surface redox processes. The surface Li-ion storage mechanism is strongly dependent on the surface area. At the same time, the capacity originated from the surface Li storage is highly reversible, which contributes significantly to the cyclability of the rutile nanoelectrode.

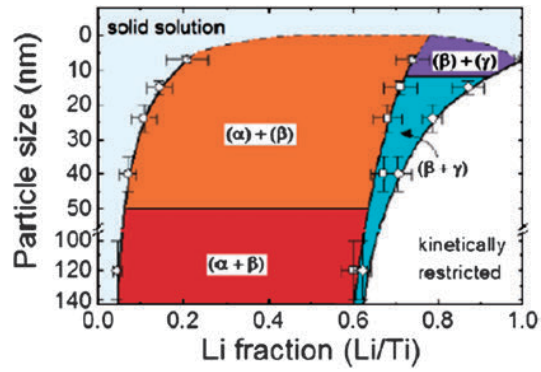

Fig. 3 Phase diagram of Li composition in anatase TiO_2 *vs.* crystal particle size based on the neutron diffraction results. R indicates the anatase phase (I_{41}/amd), α the Li-titanate phase (*Imma*) and β the $Li1TiO_2$ phase (I_{41}/amd). The different notation of the phase coexistence, for instance (R + α) or (R) + (β), reflects respectively, the coexistence or noncoexistence of the two phases within one crystalline particle. Reproduced with permission.[37]

Fig. 4 shows the size effect of rutile TiO_2 on electrochemical cycling. The Li storage capability increases greatly as the particles size decreases (that is, as the surface area increases).[38] For example, the discharge capacity of the rutile with a particle size of 300 nm (R300) is only 110 mAh g^{-1}. However, discharge capacities of 338 and 378 mAh g^{-1} are observed with particle sizes 30 (R30) and 15 nm (R15), respectively. Moreover, about 0.7 Li (264 mAh g^{-1}) per unit of rutile TiO_2 can be reversibly extracted from particles with a size of 15 nm (Fig. 4). Using ultrafine nanocrystalline rutile as the Li insertion host effectively increased the lithium storage capacity even at high discharge charge current rates due to the shortened diffusion length and increased electrolyte electrode contact area for Li^+ insertion/extraction. The capacity loss of rutile nanoelectrodes is very large in the first cycle, suggesting that full extraction of the initially inserted Li^+ ions is impossible. It is hypothesized that the slow diffusion in the *ab* planes and the Li Li repulsive interactions in the *c* direction have trapped a substantial fraction of the intercalated Li^+ ions. Similarly, nanometer-sized rutile shows a much higher electroactivity towards Li insertion than micrometer-sized rutile.[31] An excellent property of this nanometer-sized rutile is a high rate capability and even at a rate of 30 C, a reversible capacity of 70 mAh g^{-1} is maintained. (Fig. 5)

2.2. Anatase

3D networks of anatase TiO_2 consist of strongly distorted edge sharing TiO_6 octahedra with the space group of I_{41}/amd. The anatase can be considered as a stacking of 1D zigzag chains consisting of distorted edge-sharing octahedra. This stacking leads to empty zigzag channels in the anatase framework.[39] The spheres in Fig. 6 depict the possible positions of lithium ions in anatase. Filling all sites leads to stoichoimetry of $LiTiO_2$, but this is unlikely to be a real situation. Upon Li insertion, anatase converts into a two-phase mixture of tetragonal $Li_{0.05}TiO_2$ (space group I_{41}/amd) and the Li-rich orthorhombic $Li_{0.5}TiO_2$ (*Imma*).[40] The overall orthorhombic distortion of the atomic positions in the transition from anatase to lithium titanate is small and leads

Samsung Ex. 1040, Page 4 of 20
Samsung Electronics Co., Ltd., et al. v. Molecular Rebar Design, LLC
IPR2025-00356

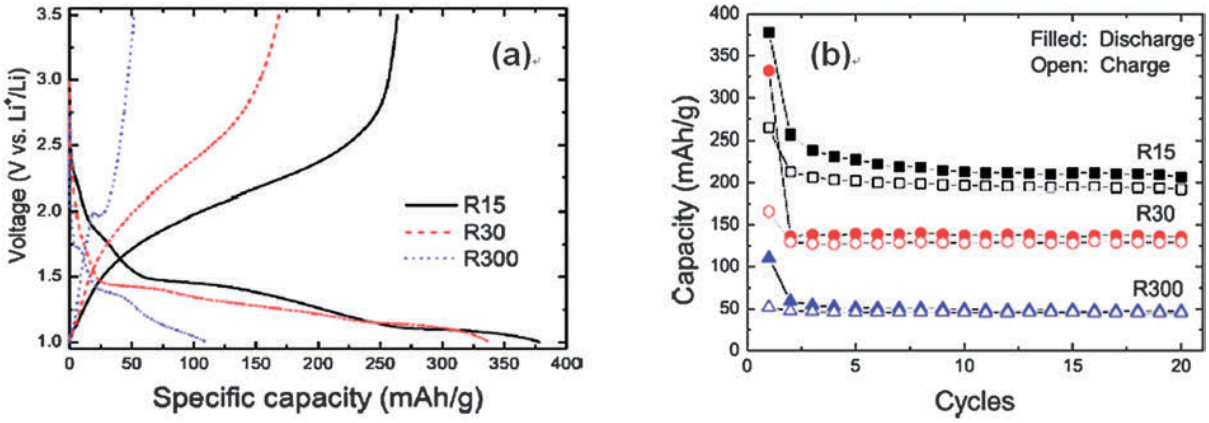

Fig. 4 (a) Voltage profiles of rutile TiO_2 with different particle sizes (R15, R30, and R300 denote the particle sizes of 15 nm, 30 nm, and 300 nm in TiO_2) and (b) capacities *vs.* cycle number in coin-type half cells at a rate of 0.05 A g^{-1}. Reproduced with permission.[38]

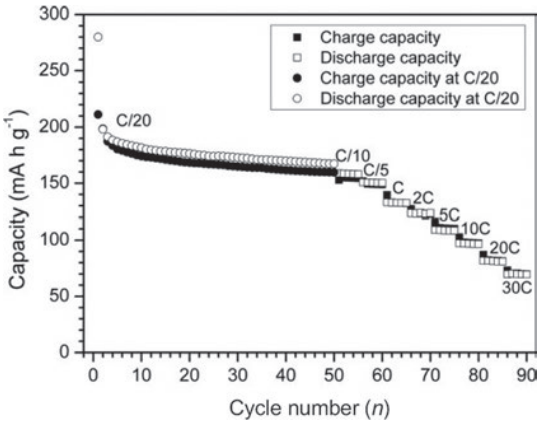

Fig. 5 Rate capabilities of TiO_2 nanoparticles with a size of 15 nm between 1 and 2.8 V at different C rates. Reproduced with permission.[31]

to more regularly shaped TiO_6 octahedra in lithium titanate than in anatase. The change in symmetry is accompanied by a decrease of the unit cell along the *c*-axis and an increase along the *b*-axis, resulting in an increase of ~4% of the unit cell volume.[41]

Among different existing TiO_2 structural types (anatase, rutile, brookite, and TiO_2(B)), studied in electrochemical cells *vs.* Li^+/Li^0, anatase presents the most interesting properties with a capacity of about 0.6 lithium ion in Li_xTiO_2 at 1.78 V *vs.* Li^+/Li. This was confirmed separately using chemical lithiation with

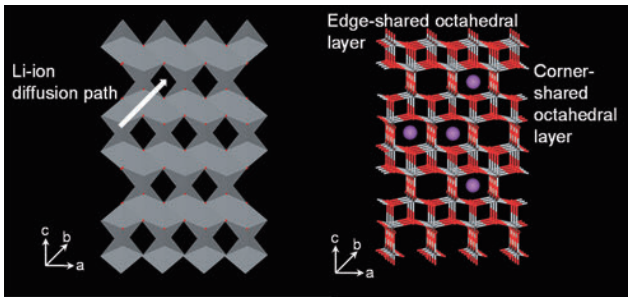

Fig. 6 Structure of anatase TiO_2.

n-butyllithium which leads to a lithium uptake of 0.7 lithium per TiO_2.[42] *Ex-situ* X-ray diffraction upon lithium insertion demonstrated the formation of $Li_{0.5}TiO_2$, which crystallizes in an orthorhombic cell having an *Imma* space group, through a two-phase transition.[43] Recently, further studies claimed that good reversibility can be achieved with nanostructured anatase TiO_2 either as mesoscopic[44,45] or nanotubes.[46] The main effect of decreasing the crystallite size is to broaden the energy levels accessible in the materials, thus leading to a broader voltage window at which the electrochemical reaction takes place.[47]

Anatase TiO_2 nanotubes were first reported by Kasuga *et al.* in the reaction of TiO_2 particles with NaOH aqueous solution. When bulk anatase TiO_2 is treated in 10 M NaOH at 120 °C, layered-structured titanates such as $Na_xTi_yO_z$ can be formed as intermediate products. During the hydrothermal process, Na^+ cations residing between edge-shared TiO_6 octahedral layers can be replaced gradually by H_2O molecules.[48,49] Intercalated H_2O molecules are larger than Na^+ ions, so the interlayer distance increases and the static interaction between neighboring TiO_6 octahedral sheets weakens. Consequently, layered titanate particles exfoliate to form nanosheets that curl up from the edges to form TiO_2 nanotubes.[50–52] The TiO_2 source used for preparing the nanotubes was commercially available rutile TiO_2 powder (particle size 0.3 μm). A mixture TiO_2 powder, NaOH, and distilled water was treated with ultrasonication for 30 min, followed by treatment at 150 °C in a Teflon-lined autoclave for 48 h.[53] After treatment, the sample was treated with a 0.1 M HCl solution and dried at 100 °C for 12 h. The dried sample was annealed further at 300 and 400 °C for 3 h. XRD pattern of peaks in the as-prepared samples at 150 °C matched well with anatase TiO_2 and layered $H_2Ti_2O_5 \cdot H_2O$.[53] $H_2Ti_2O_5 \cdot H_2O$ is a product of $Na_2Ti_2O_5$ and has a monoclinic lattice, with parallel kinked layers of edge-sharing TiO_6 octahedra. Such layers intercalate alkali metal cations, M^+, which can be further ion-exchanged with H^+ to produce protonic hydrous titanates, $H_2Ti_2O_5 \cdot H_2O$. The reaction is topotactic; hence, the protonic titanates preserve the original layered structure. However, thermal dehydration of protonic titanates leads to TiO_2 while the anatase or rutile phase grows, depending on the pretreatment conditions. Wang *et al.* reported mixed anatase and TiO_2(B) nanotubes annealed at 350 °C using 30% rutile and 70% anatase TiO_2 in a 60 mL solution of

This journal is © The Royal Society of Chemistry 2009

Samsung Ex. 1040, Page 5 of 20
Samsung Electronics Co., Ltd., et al. v. Molecular Rebar Design, LLC
IPR2025-00356

20 M NaOH (aq.) and ethanol.[54] However, Gao *et al.* reported the conversion of $H_2Ti_3O_7$ nanotubes into anatase TiO_2 nanotubes at 500 °C in an argon atmosphere, but the product showed a few rods among the tubes.[55] Anatase nanotubes showed first cycle charge and discharge capacities of 305 and 200 mAh g^{-1}, showing coulombic efficiency of 66%, and discharge capacity at a rate of 640 mA g^{-1} was 170 mAh g^{-1} and shows capacity retention of 118 mAh g^{-1} after 100 cycles.

The particle size effect was investigated with three different sizes, 6, 15, 30 nm (BET surface areas were 258, 83, and 57 m^2 g^{-1}, respectively). At rates of ~ 6 and 60 C, the charge capacities were 181 mAh g^{-1} and 139 mAh g^{-1} respectively.[56] For a given amount of anatase powder, increasing the specific surface area will inevitably increase the proportion of the total number of atoms near or on the surface, which subsequently decreases the available interstitial octahedral sites for Li insertion in the bulk anatase. Since A6 (particle size 6 nm) has the largest specific surface area among all these powders, its larger amount of surface atoms reduces the octahedral sites for Li insertion, so shortens the biphasic region on the discharge curve (plateau). As seen in Fig. 7, C_{ab} of A6 is much higher than that of A30, which is consistent with its larger specific surface area.

Despite that, C_{ab} of both electrodes only decreases slightly with increasing current density, indicating that the capacity contributed by the surface Li-ion storage is very stable and almost does not change with current density. This indicates that surface Li-ion storage depends only on surface area and not on diffusion time.[56] On the contrary, Li insertion/extraction into/from the bulk anatase is highly dependent on diffusion time since it is a solid-state diffusion process. This result indicates that the Li insertion/extraction only occurs in the outer layers of the particles at a high current rate due to the very short diffusion time. Because of the shorter Li diffusion length, most of the interstitial octahedral sites are still available for Li insertion in a very short time, therefore, A6 shows a much slower decrease of C_{bc} with the current density. This result demonstrates that, aside from increasing the specific surface area, reducing the Li diffusion length of the electrode materials is important also to facilitate Li insertion/extraction and to improve the high rate performance.

Song *et al.* reported hollow anatase TiO_2 microspheres from a template-free method based on the mechanism of Oswald ripening, differential diffusion (Kirkendall effect).[57] Compared with a similar previous attempt which also made use of Oswald ripening, their method is reported to be a one-pot template-free method without hazardous organic solvents. They prepared hollow TiO_2 at 180 °C from a reaction of $Ti(SO_4)_2$ and NH_4F. Its first discharge and charge capacities were ~295 and ~200 mAh g^{-1}, respectively, showing coulombic efficiency of 68%. However, it showed rapid capacity fading, and after 20 cycles, the capacity retention decreased to 10%. Although this material showed improved cycling stability up to 20 cycles, thereafter it showed similar capacity retention as the bulk phase. This result may indicate that micron-size TiO_2 is not effective in reducing the lattice strains induced by repetitive cycles. There are also reports of the effects of the synthesis method on electrochemical properties. Anatase TiO_2 nanowires were prepared by 10 M NaOH and 110 °C for 24 h in an autoclave, and neutralized with 0.1 mL HNO_3 and annealed at 400 °C for 4 h. The charge capacity was

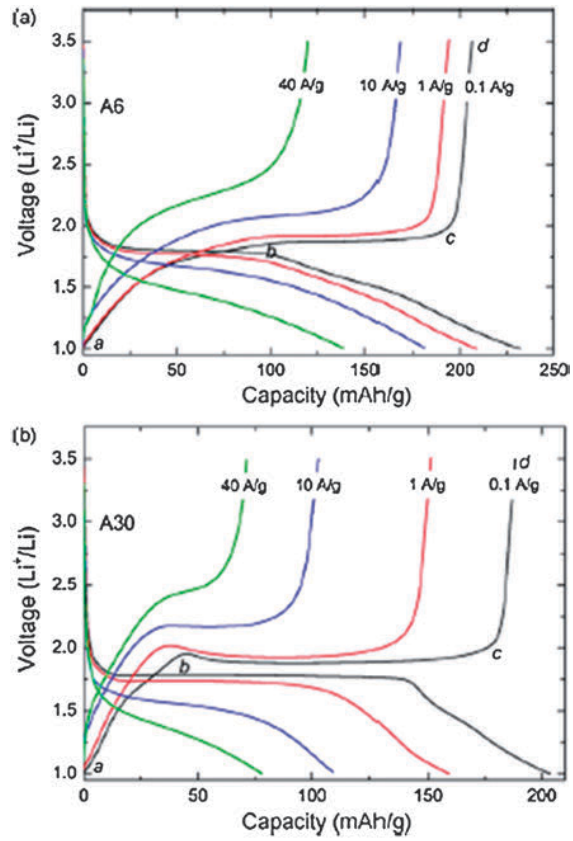

Fig. 7 Rate capabilities of anatase TiO_2 with particle sizes of 6 nm (A6) and 30 nm (A30). Reproduced with permission.[56]

239 mAh g^{-1} with a coulombic efficiency of 82% and 98% retention after 20 cycles at a rate of 36 mA g^{-1}.[58] Anatase TiO_2 nanorods from rutile powder were prepared by using 10 M NaOH and autoclave at 180 °C, followed by rinsing with HCl. In this case, titanate $TiO_2 \cdot nH_2O$ nanotubes and nanorods were obtained at 150 °C and 180 °C respectively. Upon firing at 500 °C, the nanotubes turned into anatse TiO_2 nanorods, and they showed discharge capacities of ~250 mAh g^{-1} and ~175 mAh g^{-1}.[59] TiO_2 $CdSO_4$ composite template was prepared by air-calcining Ti Cd precursors, and after treatment with dilute aqueous acid solution to remove $CdSO_4$, anatase TiO_2 was left behind. The product had large scale uniform spherical particles with an average diameter of 300 nm and exhibited BET surface area of 131 m^2 g^{-1} with various sizes of mesopores.[60] First discharge and charge capacities were 325 mAh g^{-1} and 210 mAh g^{-1} ($Li_{0.63}TiO_2$), respectively. They reported that the sloped region at the beginning may be due to Li storage in the surface region of the material.

2.3. TiO_2(B)

The framework of the idealized TiO_2(B) structure (Fig. 8) is a shear derivative of ReO_3. The molecular sheets of corner sharing (ReO_3 blocks) and edge-sharing octahedral layers are connected to each other by edge-sharing octahedra, resulting in a three-dimensional framework. When shifted by half of the unit cell length in the [100] direction, [21] TiO_2(B) shows a system of

Samsung Ex. 1040, Page 6 of 20
Samsung Electronics Co., Ltd., et al. v. Molecular Rebar Design, LLC
IPR2025-00356

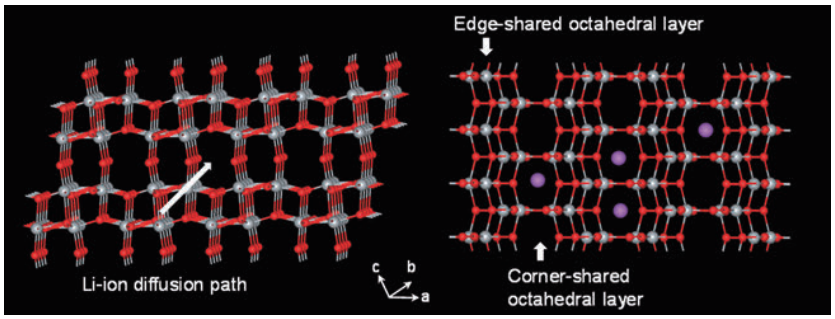

Fig. 8 Structure of TiO_2(B).

one-dimensional infinite channels in molecular sheets which follow the [001] direction. In these channels where lithium ions can be inserted the lithium ions are expected to be very mobile.[39] The maximum insertion amount of lithium ion in TiO_2(B) is about 0.85 Li per Ti at 25 °C. TiO_2(B) is the least dense polymorph of TiO_2, and has a theoretical capacity of 335 mAh g^{-1}. which makes it a superior intercalation host for lithium compared with rutile and anatase.[61] It was demonstrated that bulk layered protonated titanates could be transformed to a metastable monoclinic modification of TiO_2 (TiO_2(B)) under annealing. This modification of TiO_2 has lower density than anatase or rutile and a monoclinic unit cell. The structure of TiO_2(B) is characterized by a combination of edge- and corner-sharing TiO_6 octahedra forming a structure with channels in which transport and exchange of small cations can occur. Density ranges from 3.64 and 3.76 g cm^{-3}, which are smaller than the densities of anatase and rutile (3.9 and 4.25 g cm^{-3}).[39]

Although the TiO_2(B) nanotube and nanowire are white and insulating, they can act as a n-type semiconductor due to the reduction of the Ti^{4+} centers.[62,63] TiO_2(B) was prepared by adding TiO_2 anatase to 10 M aq. NaOH, and hydrothermally treated at 170 °C for 72 h. The product was acid-washed, which involved stirring the sample in 0.05M HCl solution for 2 h. After that it was fired at 400 °C in air. The as-synthesized TiO_2(B) nanowires had typical diameters of 20 40 nm and lengths of 2 10 μm.[62,63] The TiO_2(B) nanotubes could intercalate Li ions up to a capacity of 305 mAh g^{-1} ($Li_{0.91}TiO_2$). The reversibility after the 1st cycle was 99.8% (irreversible capacity was 33%) (Fig. 9). Previously reported data on TiO_2(B) nanowires and bulk TiO_2 are also included for comparison. Up to discharge capacity of 338 mAh g^{-1} could be inserted into the nanotubes corresponding to the composition of $Li_{1.01}TiO_2$(B), this is greater than the wires. This capacity is greater than that of the nanowires. Because the crystal structure is the same in all cases, such differences are related to the different particle dimensions and surface areas of the bulk (20 m^2 g^{-1}), nanowire (36 m^2 g^{-1}) and nanotube (190 m^2 g^{-1}) materials. Particles with higher surface areas are likely to result in electrodes with higher electrode/electrolyte contact areas. Coupled with the shorter diffusion paths within the smaller particles, this will lead to more facile intercalation in the order, tubes > wires > bulk material. Reduced strain of intercalation and contributions from charge storage at the surface may also contribute to increased Li capacity, especially in the case of tubes which exhibit the highest surface area as well as wall thicknesses for intercalation of only 25 30 Å.[62,63]

2.4. Coating

A TiO_2 host for Li-ion intercalation has intrinsically low electronic conductivity. Therefore, enhancement of electronic conductivity for the host TiO_2 material is also required to decrease the polarization. While conducting additives such as carbon black can be mechanically blended with the host material in Li-ion battery electrodes, a larger amount of conducting additives is required to obtain the desirable electronic conductivity. In general, over 10 wt% of carbon black is used in order to maintain a high rate performance. In this regard, several improvements have been made. Moriguchi *et al.* reported the preparation of single-walled carbon nanotube (SWNT)-containing mesoporous TiO_2 using a dispersed aqueous solution of cut SWNTs (c-SWNTs) as the water phase in a water/surfactant/oil ternary bicontinuous microemulsion system.[64] Although conducting additives, such as acetylene black can be mechanically mixed with the host material in conventional Li battery electrodes, it is difficult to mix such large-sized conducting additives with mesoporous host materials because the wall of the mesoporous structure is easily destroyed by conventional mixing techniques. In this regard, the methodology is to contribute to the development of high-power charging-discharging devices by providing effective paths for both ion transport and electronic conduction in electrode materials. Hence, the composite demonstrated >15% improved rate capability at a 40 C rate, compared to pristine, unmodified TiO_2.

The Maier group reported the preparation of metal@TiO_2 core shell structures: mesoporous TiO_2 spheres were mixed with 0.1 M $RuCl_3$ solution followed by heat treatment at 450 °C in O_2 so that the final RuO_2 content was 5 wt%.[65] TEM imaging showed that the 10 nm RuO_2 particles formed a 3D interconnected network over a portion of the inner surface of the mesoporous walls, which connect the carbon network on the microscale. Compared with mesoporous TiO_2 which has discharge capacity of <10 mAh g^{-1} at the 30 C rate, the RuO_2/TiO_2 composite shows ~90 mAh g^{-1}. In another development, Cho *et al.* reported the uniform coating of metallic Sn on TiO_2 nanotubes to increase the power density of the TiO_2 electrode material.[66] A thin Sn coating layer is expected to facilitate fast and stable Li-ion pathways; thereby allowing smaller amounts of conducting carbon to be used for the desired electrochemical performance.

Fig. 10 shows the TEM images of TiO_2 nanotubes prepared at 150 °C and the core shell TiO_2@Sn nanotubes. After coating with Sn, the surface morphology of TiO_2 nanotubes appears to change

This journal is © The Royal Society of Chemistry 2009

Samsung Ex. 1040, Page 7 of 20
Samsung Electronics Co., Ltd., et al. v. Molecular Rebar Design, LLC
IPR2025-00356

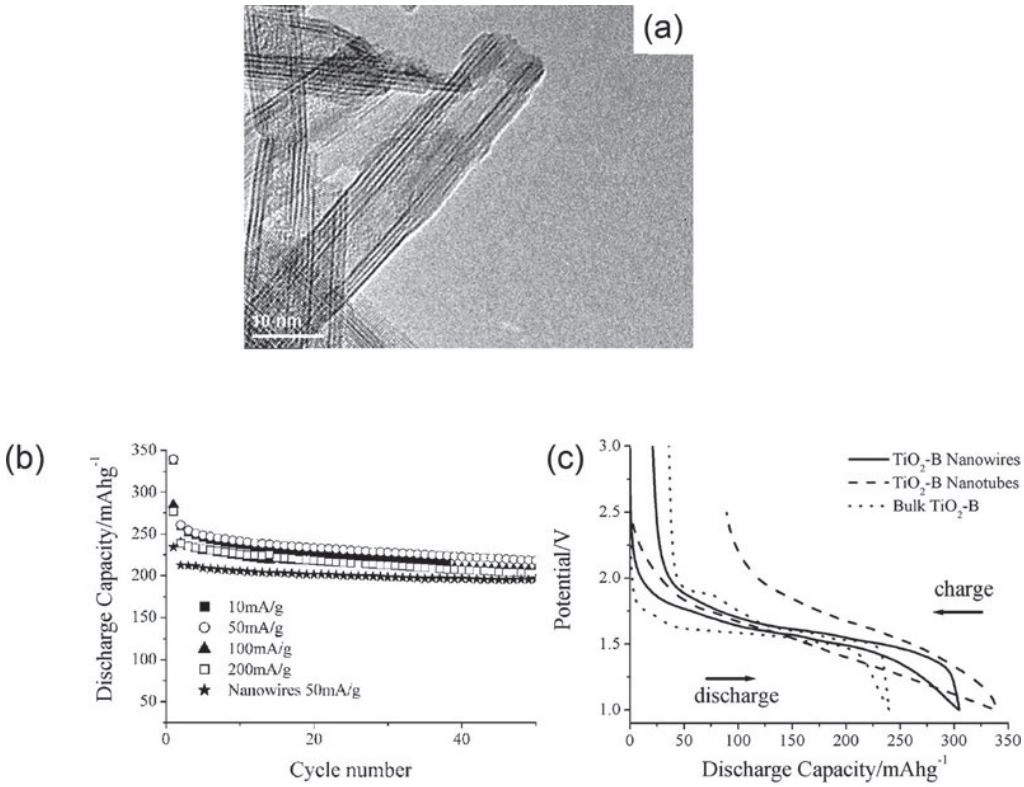

Fig. 9 (a) TEM image of TiO_2(B) nanotube, (b) rate capability of TiO_2(B) nanotube (also, its cycle life performance is compared with TiO_2 nanowires), and (c) voltage profiles of TiO_2(B) nanotube, nanowires, and bulk. Reproduced with permission.[62,63]

completely. The lattice fringes of the (200) plane correspond well with the *d* spacing of 2.91 Å of the tetragonal metallic Sn phase. As can be seen in the TEM image of an isolated nanotube, the tube diameter increases from 8.5 nm to 12 nm after Sn coating,

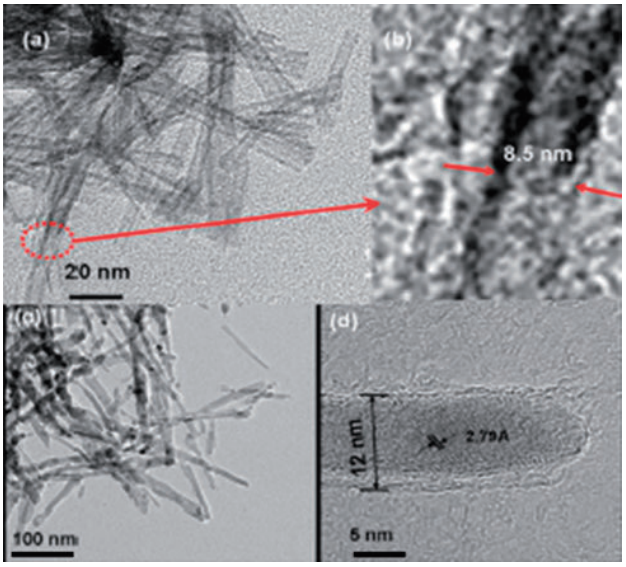

Fig. 10 TEM images of (a) TiO_2 nanotubes prepared at 150 °C and (b) high resolution image of (a), TEM images of (c) TiO_2@Sn core–shell nanotubes, and (d) high resolution image of (c). Reproduced with permission.[66]

implying that the Sn coating thickness is approximately 1.75 nm. The TiO_2@Sn electrode used only 5 wt% of carbon black, which is smaller than the mount of carbon additive required for utilizing bare TiO_2 nanotubes described above as well as in earlier reports. The electrode density in this case increased to 1.8 g cc^{-1}. The first charge and discharge capacities were 222 and 199 mAh g^{-1} respectively. The columbic efficiency of 90%, is a 40% improvement over that of the bare TiO_2 nanotubes.[66] Due to the low electronic conductivity of TiO_2, many studies have utilized large amounts (over 15 wt%) of conducting carbon black; with resultant decrease in the electrode density of the cell. However, Sn shells have an electronic conductivity in the order of $\sim 10^6$ S cm^{-1}, which is higher than carbon black ($\sim 10^2$ S cm^{-1}), and surface charge transfer reactions can be enhanced by the metallic Sn shell even with only 5 wt% of carbon black. Furthermore, Sn is only reactive below 1 V, and hence does not contribute to the measured capacity between 2.5 and 1 V. That is, the presence of Sn was just to enhance the electronic conductivity of the TiO_2 electrode material. The discharge capacity retention levels at 10 and 20 C rates were 183 and 176 mAh g^{-1}, respectively, which correspond to volumetric energy densities of 329 (183 × 1.8 g cc^{-1}) and 317 mAh cc^{-1} (183 × 1.8 g cc^{-1}), respectively. This value is improved by 3.5 times over the original value, compared to that of the bare TiO_2 nanotubes.

Fig. 11 shows O K-edge and Ti $L_{II,III}$-edge near edge X-ray absorption fine structure (NEXAFS) of the TiO_2 and TiO_2@Sn nanotubes during the first cycle in different voltage regions. The NEXAFS does not show the bulk structure of the absorbing material as the penetration depth of the soft X-ray is ~ several

Samsung Ex. 1040, Page 8 of 20
Samsung Electronics Co., Ltd., et al. v. Molecular Rebar Design, LLC
IPR2025-00356

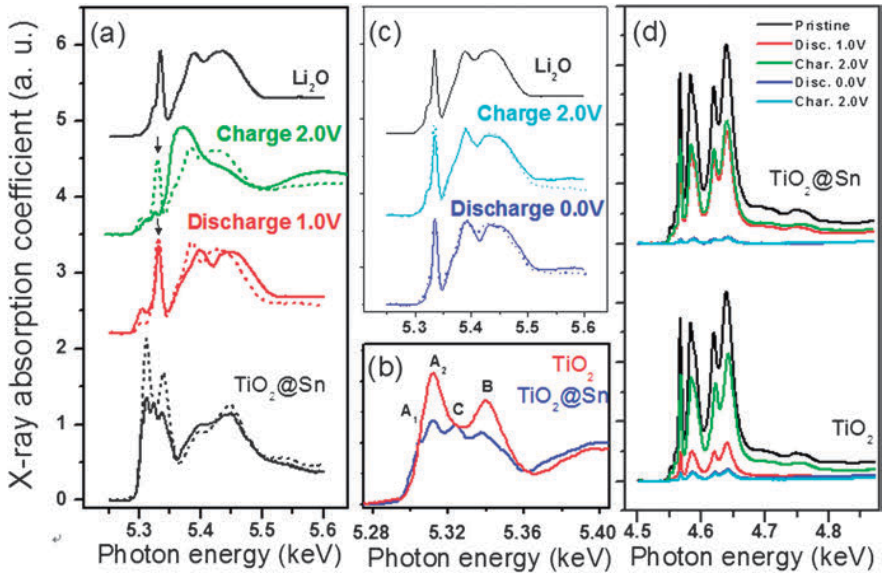

Fig. 11 (a) Oxygen K-edge and (d) Ti $L_{II,\ III}$-edge NEXAFS spectral variations of TiO_2 (dashed line) and TiO_2@Sn (solid line) nanotubes during the two different electrochemical reactions in the voltage regions of (a) 2.0 1.0 V and (b) 2.0 0.0 V. For clarity, magnified pre-edge peak features of the pristine TiO_2 and TiO_2@Sn nanotubes are presented (b) in the figure.[66b]

nanometers from the surface. Therefore, the NEXAFS can provide information concerning variations of the chemical composition in the nanotube surface region during the electrochemical Li-ion reaction. The bare TiO_2 nanotubes typically show two well-separated peaks (peaks A_2 and B) in the pre-edge region, which correspond to electric dipole-allowed transitions into hole states (2p$\underline{L}$) in oxygen 2*p* orbitals (Ti t_{2g} O 2*p* and Ti e_g O 2*p*, respectively) hybridized with 3*d* orbitals under TiO_6 octahedral symmetry. The broad higher energy peaks above 535 eV can be assigned to transitions to hybridized states of oxygen 2*p* and Ti 4*sp* orbitals. For the TiO_2@Sn, on the other hand, Sn-coating leads to new peaks A_1 and C, which correspond to the pre-edge peaks of the oxygen ions preferentially coordinated to Ti and Sn atoms for rutile-like Sn Ti O mixed phase, respectively.[67] The existence of the rutile-type Ti Sn O phase is in a good agreement with the Ti K-edge EXAFS results.

Upon discharging to 1.0 V, the overall pre-edge peak intensities of TiO_2 and TiO_2@Sn nanotubes decrease abruptly and a sharp peak feature is formed at 5.34 keV (denoted by ↓). The decrease of the pre-edge peak intensity implies a decrease of the hole state in the oxygen 2*p* band; specifically, a greater reduction of bond covalency in Ti O bonding pair occurs due to chemical reduction of the oxygen ion from $O^{-2+\delta}$ to the O^{-2} state, where the δ value is the degree of hole state in the oxygen 2*p* orbital and is proportional to the covalent bonding character. Additionally, the new peak at 534 eV is very similar to the feature of a reference Li_2O phase, which is believed to be associated with formation of an electrochemically inactive Li_2O phase on the highly active TiO_2 nanotube surfaces. Therefore, Li-ion insertion into the TiO_2 nanotubes give rise to local bond cleavage of Ti O bonding and the formation of oxygen vacancies on the nanotube surface. The inserted Li-ions can be chemically bonded with the oxygen generated from the TiO_2 nanotubes. For the TiO_2@Sn nanotubes, however, the pre-edge peak feature characteristics of the TiO_6 environment is still detectable at discharge to 1.0 V, compared to the bare TiO_2 nanotubes. Conversion reactions involving Li_2O have also been reported in 3*d* transition metal oxide systems, such as CoO, FeO and CuO which can be reversibly reduced and oxidized together with the formation and destruction of lithium oxide respectively:[19]

$$M^{II}O + 2Li^+ + 2e^- \leftrightarrow Li_2O + M^0$$

It is believed that the metallic Sn/rutile-type Sn Ti O outer bilayer prevents Ti O bonding in the inner shell from being pulverized and following the generation of the Li_2O phase on the nanotube surface during the charge. The deduction is also corroborated by the Ti L-edge NEXAFS spectra (Fig. 10d). The peak intensity after discharging to 1.0 V is relatively constant in TiO_2@Sn nanotubes, while an abrupt decrease of peak intensity was observed in bare TiO_2 nanotubes. This can be explained by the fact that the Sn-coating layer could uptake the inserted Li-ion in preference to the inner TiO_2 nanotubes and so inhibits the formation of the Li_2O phase in the inner part of the TiO_2 nanotubes. The proposed mechanism is illustrated in Fig. 12.

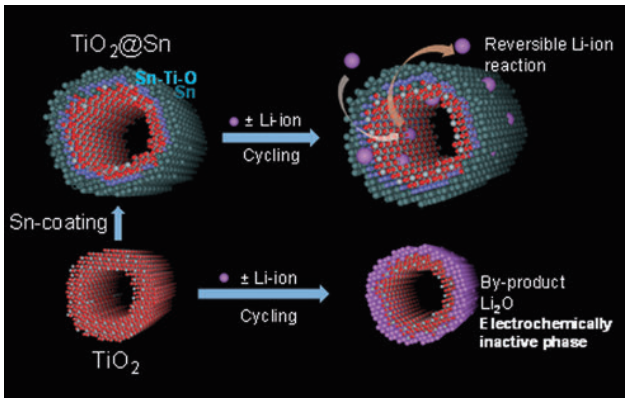

Fig. 12 Electrochemical Li-ion behavior of bare TiO_2 and TiO_2@Sn nanotubes in the voltage region between 2.0 and 1.0 V.

This journal is © The Royal Society of Chemistry 2009

Samsung Ex. 1040, Page 9 of 20
Samsung Electronics Co., Ltd., et al. v. Molecular Rebar Design, LLC
IPR2025-00356

Upon charging to 2.0 V, the TiO_2@Sn nanotubes show quite different peak features from bare TiO_2. For Li-ion extraction, TiO_2@Sn nanotubes revert to characteristics of the TiO_2 phase although the peak intensity decreases abruptly, while the peak features of bare TiO_2 remain as fixed as those of the Li_2O phase. The following inferences can therefore be made: formation of an electrochemically-inactive Li_2O phase on the bare TiO_2 nanotubes intercepts the reversible Li-ion pathway in the charging process. On the other hand, the electrochemically-active Sn/Sn Ti O bilayer in the TiO_2@Sn nanotube functions as a stable molecular membrane for Li-ion insertion and extraction processes and assists the reversible Li-ion behavior. In consequence, these results are shown in Fig. 12.

Finally, another related titania anode candidate is nanocrystalline lithium titanium oxide (LTO, *e.g.* $Li_4Ti_5O_{12}$) with a spinel structure, where the Li-ion insertion and extraction reactions occur with very little lattice expansion/contraction ("zero strain" property).[68] The voltage profile of the $Li_xTi_5O_{12}$ anode exhibits a very stable flat plateau at 1.55 V, eradicating any possibility of dendritic lithium formation. The material therefore exhibits excellent cyclability and good safety features. However, similar to the TiO_2 anodes, the problems of low energy density, poor electronic conductivity and low operating voltage remain.

3. Sn-based materials

3.1. SnO_2 nanostructured anode materials

Wide-band semiconducting SnO_2 is useful for a diverse range of applications. It is believed that some applications may benefit from a properly designed SnO_2 nanostructure. For LIBs, SnO_2 has been considered as a high capacity anode material since early 1997. However, its high capacity is undermined by poor cyclability in applications that continues to beset the material even up to today. Nanostructured SnO_2 has been proposed as a possible solution.[28,69–74] Although many SnO_2-based anode materials have been synthesized, it is still intellectually stimulating and technologically important to fabricate higher-order nanostructures and to explore their properties in applications, while keeping the methods of preparation relatively simple and scalable. Template-assisted methods, especially those using hard templates, offer the most direct approach to structure control. The formation mechanism of the product is also the easiest to understand. Template-free synthesis methods, when properly designed, can offer scalability and simplicity in implementation, although the product morphology and structure cannot be determined *a priori*.

Template-assisted synthesis is commonly used for the fabrication of high-order nanostructured materials because of its relatively simple principles and fabrication procedures (Fig. 13). There are two operational variations depending on whether active or passive templates are involved. The passive template-assisted methods employ sacrificial templates to help the organization and aggregation of precursor nanoparticles into the desired nanostructures, and then the templates are removed (Fig. 13I). In some cases the nanoparticles could undergo further transformations (*e.g.* sintering, oxidization) during the template removal process (*e.g.* by calcination) to form products with the desired chemistry and structure (Fig. 13II). The template removal process is often aggressive, and can inflict a certain amount of damage to the organized high-order nanostructures. In the active template-assisted methods, the template and the dispersed nanoparticles are formed together *in-situ*. The template removal process is constructive as it helps to shape the product morphology, including the creation of an interior structure under the right conditions (Fig. 13III). These procedures may be run in combination or recursively to produce products with the desired morphology and application properties.[28,70]

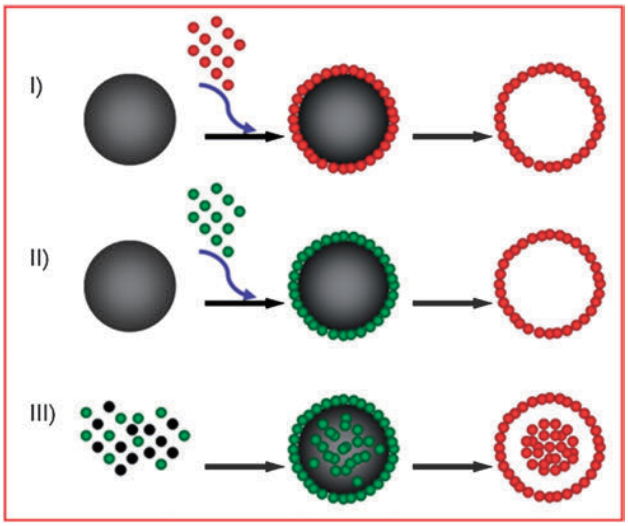

Fig. 13 Illustration of template-assisted methods in the fabrication of hollow SnO_2 nanostructures. *NB* spheres are used as the template geometry in the illustration but the principle may also be applied to other geometries such as tubes, rods, cubes and pyramids.

3.2. Active template-assisted fabrication

An active template-assisted method was used for the fabrication of SnO_2 nanoparticle aggregates with an unique mesoscale hollow core shell structure for LIB applications.[28] In this method, carbon mesospheres dispersed with crystalline SnO_2 nanoparticles were formed as the sole product of a solvothermal procedure using glucose and $SnCl_4$ in a water/ethanol mixture as the starting materials. The carbonization of glucose and the hydrolysis of $SnCl_4$ occurred simultaneously under solvothermal conditions to form the carbon mesospheres with dispersed SnO_2 nanoparticles *in-situ* (Fig. 14f). Subsequent calcination compressed the SnO_2 nanoparticles into stable hollow core shell mesospheres (Fig. 14a e). Here the carbon mesospheres from the solvothermal carbonization of glucose played a constructive role in templating the final SnO_2 morphology during the carbon removal by calcination. This method of preparation is simple, low cost, and can be conveniently scaled up for volume production.

The hollow core shell mesospheres of crystalline SnO_2 nanoparticle aggregates showed very high first cycle charge (lithiation) and discharge (de-lithiation) capacities of 2358 and 1303 mAh g^{-1} respectively (Fig. 15a). The exceptionally high first cycle charge capacity was attributed to solid electrolyte interphase (SEI) formation and the reduction of SnO_2 to Sn (eqn 1). In addition the microscopic voids in the cores and shells of the

Samsung Ex. 1040, Page 10 of 20
Samsung Electronics Co., Ltd., et al. v. Molecular Rebar Design, LLC
IPR2025-00356

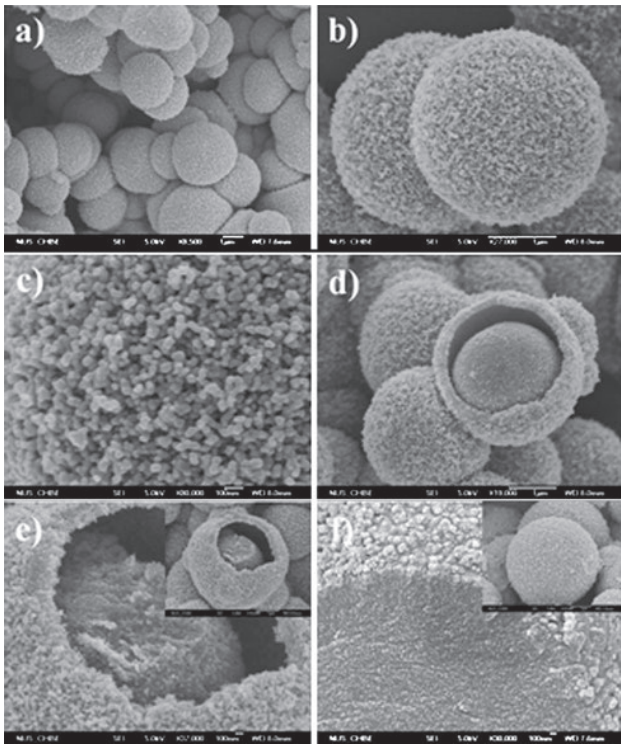

Fig. 14 FESEM images: (a–b) hollow core–shell mesospheres of crystalline SnO_2 nanoparticle aggregates; (c) zoomed-in view of the surface of a SnO_2 mesosphere; (d) a SnO_2 mesosphere with broken shell; (e) another partially broken mesosphere showing the core and shell made up of the nanoparticle aggregates; the inset is the corresponding low-magnification view; (f) zoomed-in and zoomed-out (inset) views of the solvothermal product of carbon mesospheres with dispersed SnO_2 nanoparticle precursor before calcination. Reproduced with permission.[28]

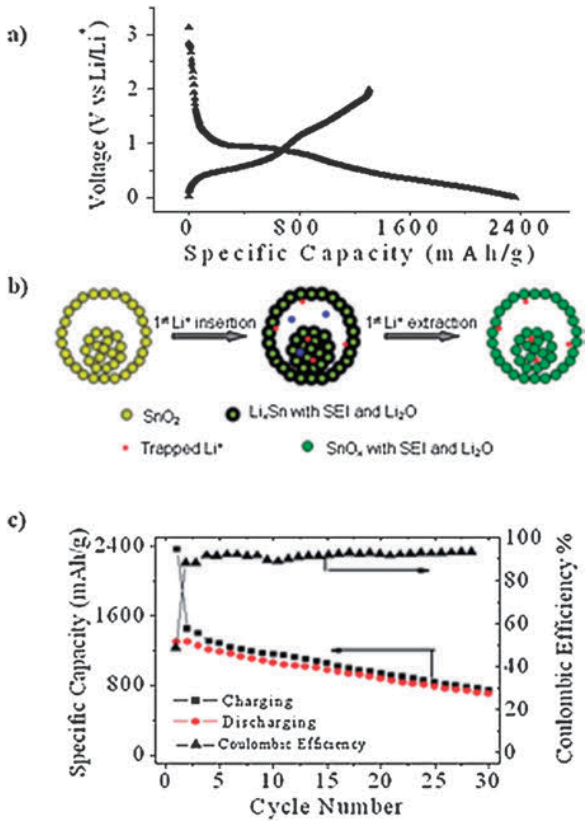

Fig. 15 (a) First cycle charge/discharge curves. (b) Schematic showing the processes occurring in the first cycle Li^+ insertion and extraction reactions. (c) Specific capacity *vs.* cycle number plots of electrodes prepared from the hollow core–shell mesospheres of crystalline SnO_2 nanoparticle aggregates. Reproduced with permission.[28]

mesospheres were also facilities for Li^+ storage. The Li^+ stored in these locations were however more difficult to extract, accounting for the large discrepancy between the charge and discharge capacities (Fig. 15b). The cycling test of SnO_2 mesospheres showed notable capacity fading. However, the extent of which was not as high as in the case of discrete SnO_2 nanoparticles. Examination of the electrode after cycling revealed partial retention of the mesosphere morphology.

3.3. Passive template-assisted fabrication

One-dimensional SnO_2 nanotubes were prepared by a passive template-assisted method using an anodic alumina oxide (AAO) membrane as the hard template.[73] Commercially available SnO_2 nanoparticles were infiltrated into the membrane channels and calcined to a dense packaging of SnO_2 nanoparticles on the walls of the AAO membrane. Subsequently the AAO template was removed by NaOH. The as-synthesized SnO_2 nanotubes were uniform in diameter, polycrystalline with SnO_2 nanoparticles as the basic building blocks (Fig. 16). The SnO_2 nanotubes showed substantial improvements in electrochemical performance over unorganized nanoparticles. The organization of the SnO_2 nanoparticle into a tubular structure was found to withstand the stress induced by repeated charge and discharge reactions, better possibly through the ability to expand and contract concentrically. In contrast, primary SnO_2 nanoparticles without any organization would pulverize severely and lose electrochemical activity over cycling for the same period of time. The specific capacity was 525 mAh g^{-1} at the end of the 80th cycle (Fig. 16).[73]

In some cases the hard template may not induce the formation of the product directly because of incompatibility issues with the starting materials or the template removal procedure may completely destroy the product. Under these situations the use of two or more sacrificial templates is necessary. The fabrication of polycrystalline hollow SnO_2 spheres serves as a good example (Fig. 17a).[74] Here the SnO_2 hollows spheres could not be formed on the primary template of silica spheres since the removal of the latter by HF would also remove SnO_2. To circumvent this, a secondary template of hollow carbon spheres was fabricated from the primary silica template. Carbon was coated on the silica spheres by chemical vapor deposition (CVD) using benzene as the carbon source at high temperatures. The silica templates were then removed by the HF treatment. SnO_2 nanoparticles (1 3 nm) were then deposited on both the external and internal surfaces of the hollow carbon spheres through infiltration. Calcination in air at 800 °C removed the hollow carbon spheres and compacted the SnO_2 nanoparticles into polycrystalline SnO_2 hollow spheres (Fig. 17b). This method of preparation of hollow spheres may be extended to other materials. It was found that the polycrystalline

This journal is © The Royal Society of Chemistry 2009

Samsung Ex. 1040, Page 11 of 20
Samsung Electronics Co., Ltd., et al. v. Molecular Rebar Design, LLC
IPR2025-00356

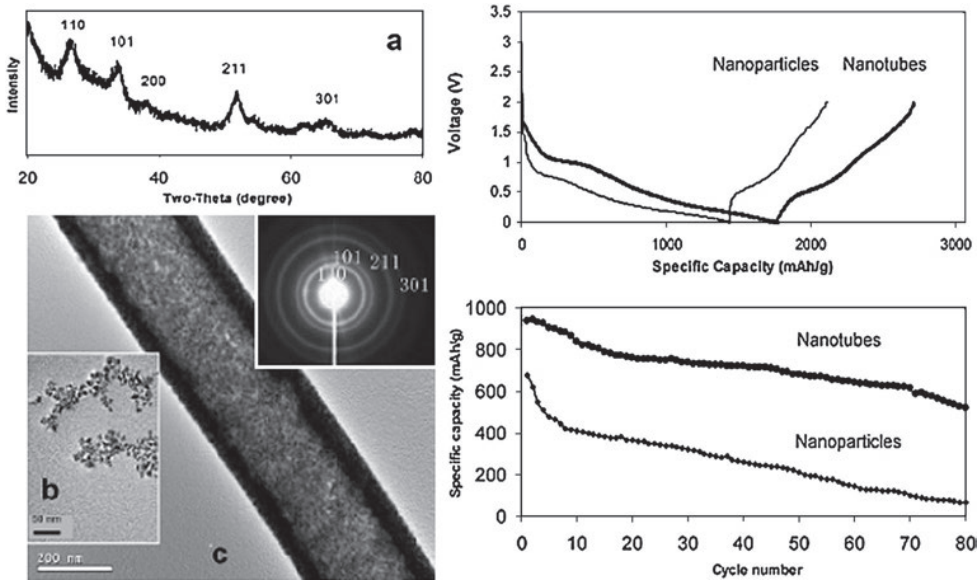

Fig. 16 The microstructure and electrochemical performance of the SnO_2 nanotubes prepared by AAO template-assisted infiltration method. Reproduced with permission.[73]

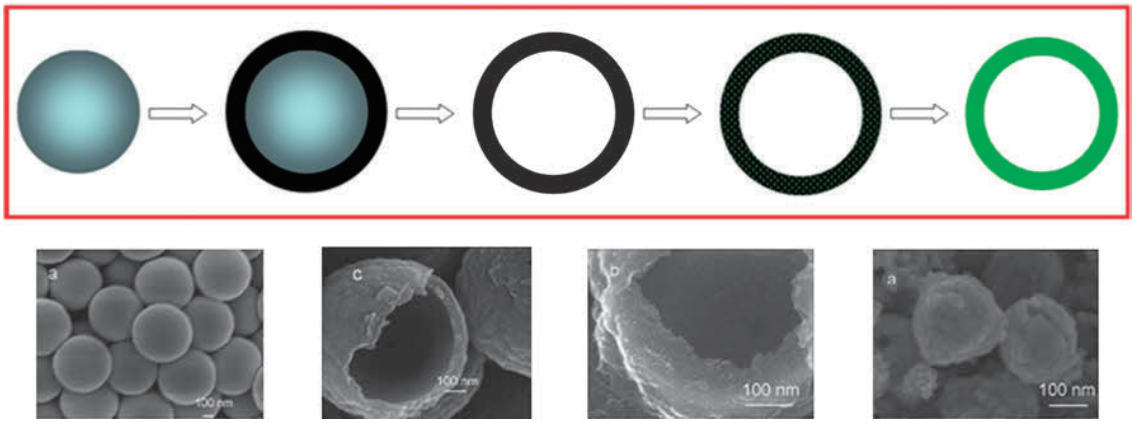

Fig. 17 (a) A two-step passive template-assisted method to fabricate the desired hollow nanostructure. (b) FESEM images (from left to right) of silica sphere template, hollow carbon spheres, SnO_2 nanoparticle-loaded hollow carbon spheres, and polycrystalline SnO_2 hollow spheres. (b) Reproduced with permission.[71]

SnO_2 hollow spheres prepared in this way still experienced significant capacity fading. On the other hand, the intermediate SnO_2 nanoparticle-loaded hollow carbon spheres sintered at moderate temperatures showed much better cyclability,[71] hinting that a compositing approach may be a more viable option for ameliorating the capacity fading problem of Sn.

Other mesoporous SnO_2 morphologies are also obtainable using hard templates which are mesoporous in nature,[75] for example cubic KIT-6 and hexagonal SBA-15 silica. The preparation involved two cycles of impregnation with $SnCl_4$ precursor and drying. After calcination, the silica template was removed by treatment in dilute NaOH. The as-synthesized mesoporous SnO_2 showed very desirable electrochemical performance (Fig. 18), which was attributed to the regular porosity which enabled thorough flooding of the electrolyte, and voidage in the mesopores for buffering volume expansion.[75]

3.4. Template-free fabrication

Template-free fabrication can be an alternative to the preponderance of template-assisted methods. By comparison template-free synthesis is relatively simple and scalable. Recently a molten salt synthesis was used to fabricate SnO_2 nanorods.[76] In this method, metallic tin nanoparticles were first formed by the chemical reduction of $SnCl_4$ in aqueous solution in the presence of a strong complexing ligand, 1,10-phenanthroline. The tin nanoparticles were then mixed with NaCl and KCl, and calcined in air at 700 °C. The resultant SnO_2 nanorods were about 15 nm in diameter with high aspect ratios ranging from 50 100 (Fig. 19). The one-dimensional SnO_2 nanorods with high aspect ratios could present advantages for enhanced Li^+ diffusion and extra storage of Li^+ ions in the space between stacks of nanorods. A more popular route to template-free synthesis of SnO_2

Samsung Ex. 1040, Page 12 of 20
Samsung Electronics Co., Ltd., et al. v. Molecular Rebar Design, LLC
IPR2025-00356

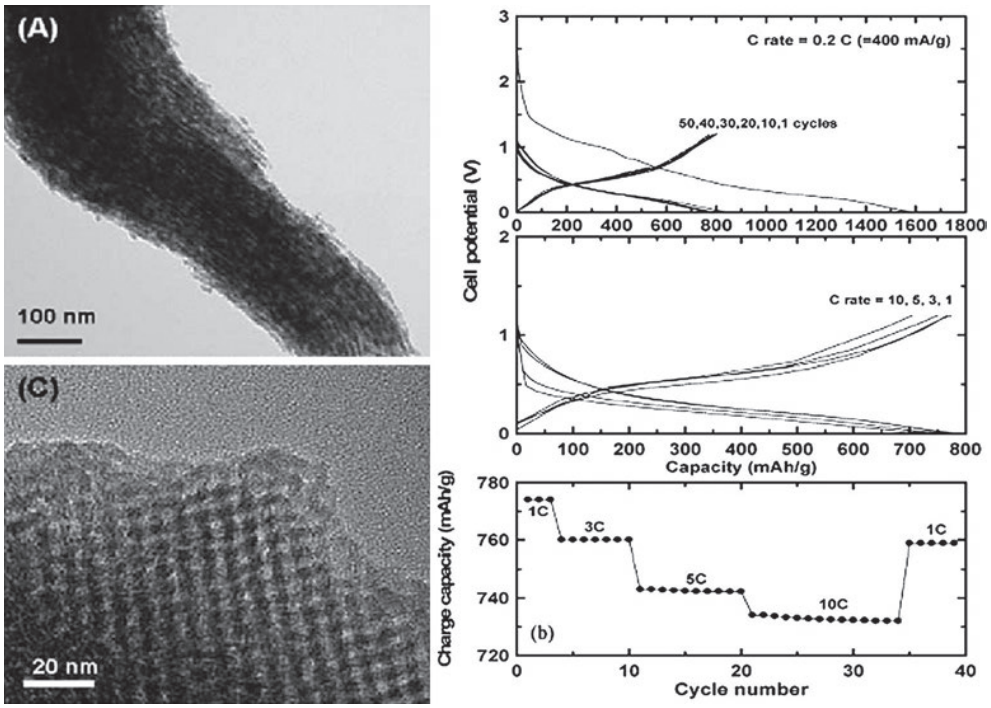

Fig. 18 TEM images of as-prepared mesoporous SnO_2 (left) and the electrochemical performance of the mesoporous SnO_2 (right). Reproduced with permission.[75]

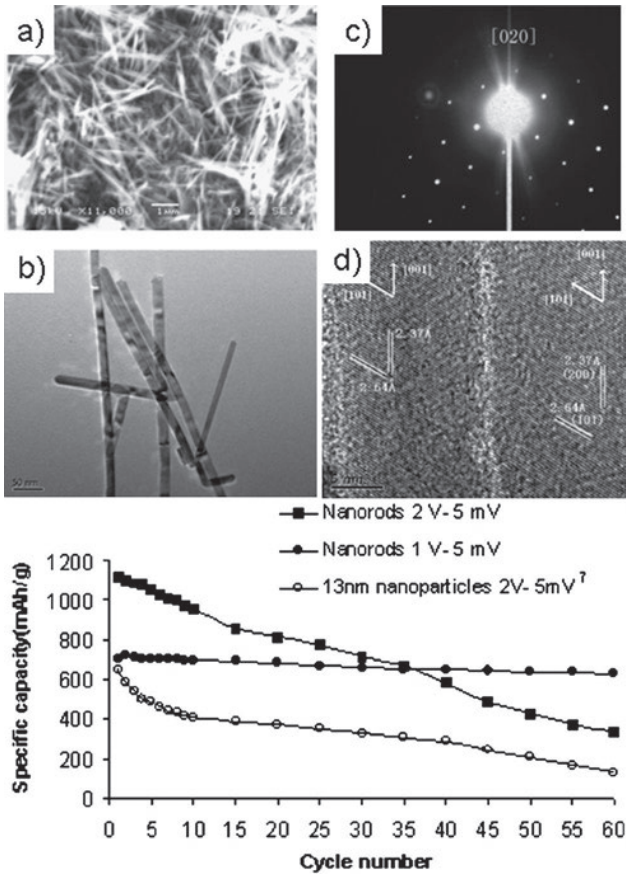

Fig. 19 SnO_2 nanorods from molten-salt synthesis and calcination in air and their cycling performance. Reproduced with permission.[76]

nanostructures is hydrothermal synthesis. A notably simple fabrication procedure was reported recently.[72] In this procedure the hydrothermal treatment of potassium stannate trihydrate with the chemical addition of urea in a formulated water ethanol mixture can lead to the formation of hollow or core shell SnO_2 spherical nanostructures; depending on the experimental conditions (Fig. 20).[72] Template-free formation of hollow nanostructures was rationalized by Ostwald ripening. This method of preparation of SnO_2 nanostructure is simple and scalable. Electrochemical tests indicated highly improved Li^+ ions storage properties which could be attributed to the unique hollow nanostructure.[72]

Another interesting SnO_2-based anode material is electrospray deposited thin films of particles with a unique porous spherical multideck-cage morphology (Fig. 21a).[77] Besides morphology, the authors were also able to vary the composition of the deposited thin films from SnO_2 to Li_2O SnO_2, CuO SnO_2 and Li_2O CuO SnO_2. All of the as-prepared thin film electrodes showed good electrochemical performance, especially for the Li_2O CuO SnO_2 film. Reversible capacity was reported to be as high as 1158 mAh g^{-1} (Fig. 21b). The improved electrochemical performance was attributed to the unique structure and the presence of Li_2O and CuO phases in the composite film.[77] However, there are issues of high cost and scalability for production since film thickness is limited to 10 15 μm. The above examples illustrate that a high-order SnO_2 nanostructure could be used to deliver a higher level of performance because of morphologically-enhanced properties, and reversibility. However, the first cycle capacity loss due to the reduction of SnO_2 to Sn and SEI formation remains significant. In addition, capacity fading is still prominent in most SnO_2 nanostructured

This journal is © The Royal Society of Chemistry 2009

Samsung Ex. 1040, Page 13 of 20
Samsung Electronics Co., Ltd., et al. v. Molecular Rebar Design, LLC
IPR2025-00356

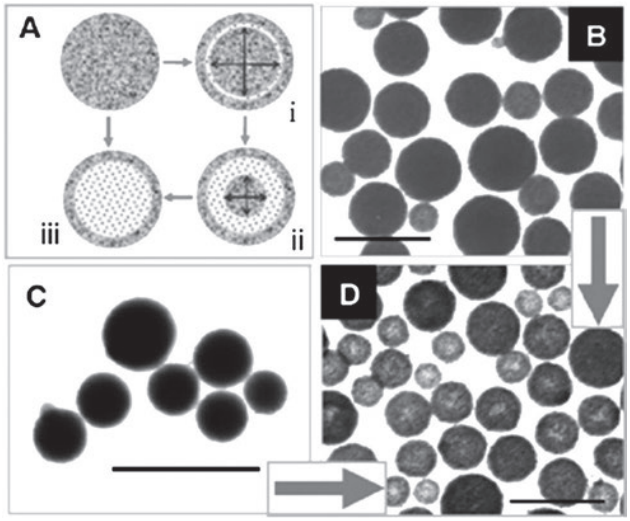

Fig. 20 TEM images of SnO_2 nanostructures obtained by hydrothermal treatment of stannate with chemical addition of urea. SnO_2 spheres prepared from the hydrothermal treatment of stannate with the chemical addition of urea: (a) Schematic illustration of the proposed inside-out ripening mechanism. Typical TEM image of (b) SnO_2 nanospheres obtained with 6 h of reaction at 150 °C, and (c) amorphous SnO_2 nanospheres obtained by ageing. (d) Typical TEM image of hollow SnO_2 nanospheres prepared from the SnO_2 nanospheres in (b) or (c). All scale bars are 500 nm. Reproduced with permission.[72]

materials. Morphology aside, there is also an upper limit on the size of a particular SnO_2 nanostructure to show promising performance.[78] The current morphological modifications and size control methodologies have rectified some, but not all of the SnO_2 deficiencies in applications.

3.5. SnO_2/C composite nanostructured anode materials

Instead of using phase-pure SnO_2 nanostructures, one could form composites of SnO_2 and carbon at the nanoscale to leverage upon the high capacity of SnO_2 and the good cyclability of carbon. Depending on the quality and quantity of carbon used, the composite could be treated as a dual host storage system for Li^+ ions or the presence of carbon is merely to relieve the stress-induced pulverization problem of SnO_2. The SnO_2/C composites may be prepared by a variety of methods, ranging from simple direct deposition of SnO_x nanoparticles on graphite (KS6) surface,[79,80] to the *in-situ* formation of SnO_2-laden carbon mesospheres,[28] template-assisted fabrications of ordered mesoporous carbon loaded SnO_2 composites[81] and carbon nanotube (CNT)-encapsulated SnO_2.[72]

The CNT-encapsulated SnO_2 nanotubes warrant a special mention as they represent one of the best efforts so far. They were prepared by treating SnO_2 nanotubes with CVD of CNTs.[70] Polycrystalline SnO_2 nanotubes with uniform diameter were formed first by the infiltration method described earlier. Subsequent CVD treatment of the SnO_2 nanotubes in an AAO membrane using acetylene as the carbon source led to the encapsulation of the SnO_2 nanotubes by a thin layer of CNTs (Fig. 22). The CNT skin provides good electrical contact, and

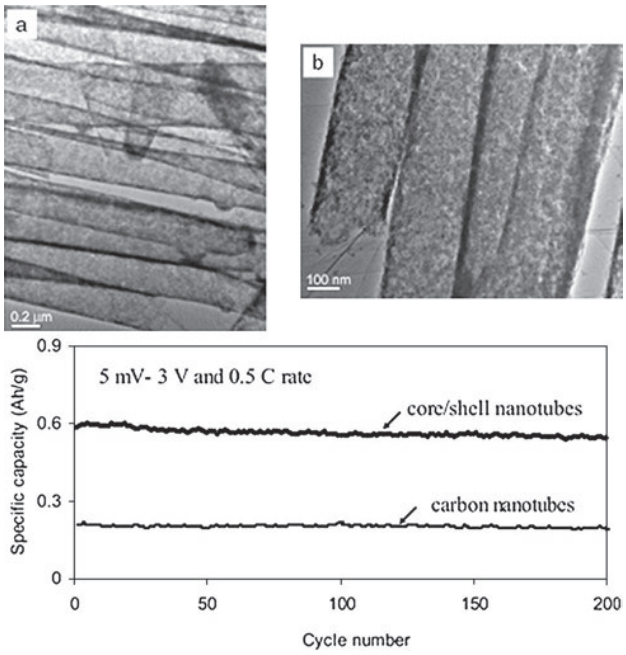

Fig. 22 CNT-encapsulated polycrystalline SnO_2 nanotubes and their cycling performance. Reproduced with permission.[70]

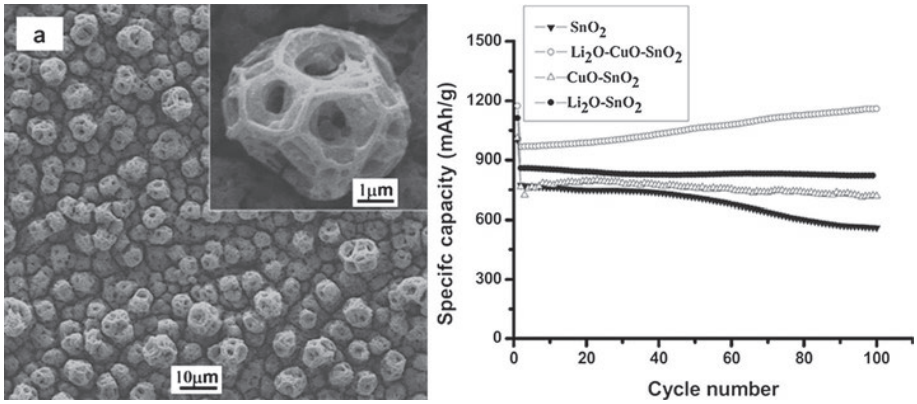

Fig. 21 SEM images of the as-deposited film of nanostructured SnO_2 on copper current collector (a). Specific capacity *vs.* cycle number plots of Sn-based multideck-cage particles films with different compositions (b). Reproduced with permission.[77]

Samsung Ex. 1040, Page 14 of 20
Samsung Electronics Co., Ltd., et al. v. Molecular Rebar Design, LLC
IPR2025-00356

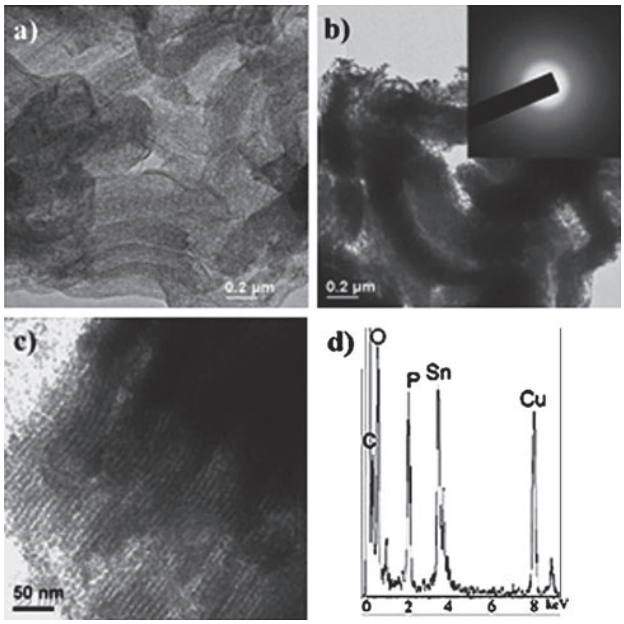

Fig. 23 TEM images of CMK-3 mesoporous carbon (a) and ordered nanostructured SnO_2/C composite at (b) low and (c) high magnifications. Reproduced with permission.[81]

could absorb the reaction-induced stress by using the space in the open tubular structure for free material expansion. This SnO_2/C composite nanostructure showed excellent cycling behavior (Fig. 22).[70] An SnO_2/C composite was also prepared by mixing $SnCl_2$ with phosphorus esters in the presence of ordered mesoporous carbon (CMK-3, prepared from SBA-15 silica template) to deposit tin oxides into the 3-dimensional nanospace of mesoporous carbon. The composite was subsequently aged at 40 °C and then at 900 °C before calcination in air at 500 °C (Fig. 23). The 3-dimensional carbon framework was believed to inhibit aggregation of the tin and hence it improved cycling performance compared with unsupported SnO_2 nanoparticles.[81]

In-situ fabrication of SnO_2/C without a template could offer a simple and scalable production of the composite anode materials.[28,82–84] Such *in-situ* fabrication techniques are often based on the carbonization of carbohydrates (*e.g.* glucose) and the pyrolysis of a tin precursor (*e.g.* $SnCl_4$) under the high temperature and pressure conditions prevalent in a solvothermal synthesis. It was found that the selection of solvent is crucial for morphology control of the SnO_2/C product. For example, the product was random SnO_2 nanoparticles coated with disordered carbon when the solvent was water or ethylene glycol.[28,83,84] On the other hand, ethanol or ethanol water mixture formed carbon mesospheres with dispersed SnO_2 nanoparticles (Fig. 24).[28,82] Since the carbonization temperature is relatively low in a solvothermal synthesis, only poorly graphitized disordered carbon abundant with active surface groups can be formed. This type of carbon is not suitable for reversible storage of lithium ions.

3.6. Sn/C composite nanostructured anode materials

If Sn is used as the Li storage compound, eqn (1) would not occur and the coulombic efficiency should in principle be higher. Metallic Sn also has the highest theoretical storage capacity of any Sn anode (993 *vs.* 782 mAh g^{-1} for SnO_2). In reality, however, the pulverization problem is aggravated because of the lack of a protective buffering matrix to moderate volume excursion.[85,86] The use of Sn may be improved by compositing Sn with carbon at the nanoscale. If properly designed, a Sn/C composite could combine the high specific capacity of Sn with the good cycle life of carbon. At the same time one should however be mindful of the corresponding increase in interfacial passivation leading to permanent loss of usable capacity.[87] A prudent material design should therefore provide a good balance of these opposing features. Previous work in our lab, and by others, on nanostructured Sn/C composite anode materials have shown some encouraging results.[84,85,88–90] However, the fabrication of nanostructured Sn/C composites by simple and scalable methods poses an even greater challenge. There are four general methods available to prepare a Sn/C composite, namely the deposition of pre-formed Sn nanoparticles on graphite,[90] coating of Sn nanoparticles with thin, nanoscale layers of carbon,[91,92] the *in-situ* reduction of SnO_2 to Sn in carbon[94] and template-assisted synthesis.[93] A few representative examples of these fabrication techniques are provided.

The loading of Sn nanoparticles on carbon is a relatively straightforward procedure. For example, by using $SnCl_4$ as the Sn precursor, 1,10-phenanthroline as the complexation and capping agent, and $NaBH_4$ as the reducing agent, Sn nanoparticles 3.5 and 10 nm in diameter could be prepared in aqueous solution.[95] In the presence of carbon (KS-6), the Sn nanoparticles could be deposited selectively on graphite (KS-6) after

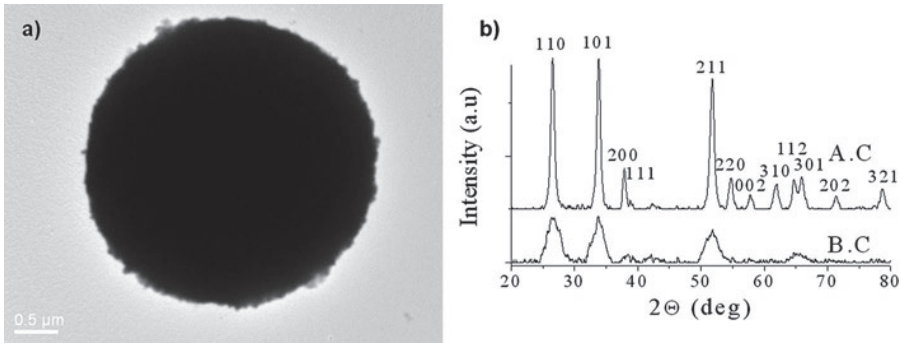

Fig. 24 TEM images of typical carbon mesopheres loaded with SnO_2 nanoparticles (~3.5 nm). (a) XRD patterns of SnO_2/C composite mesospheres before calcination (lower) and after calcination in air to remove the carbon (upper). Reproduced with permission.[28]

This journal is © The Royal Society of Chemistry 2009

Samsung Ex. 1040, Page 15 of 20
Samsung Electronics Co., Ltd., et al. v. Molecular Rebar Design, LLC
IPR2025-00356

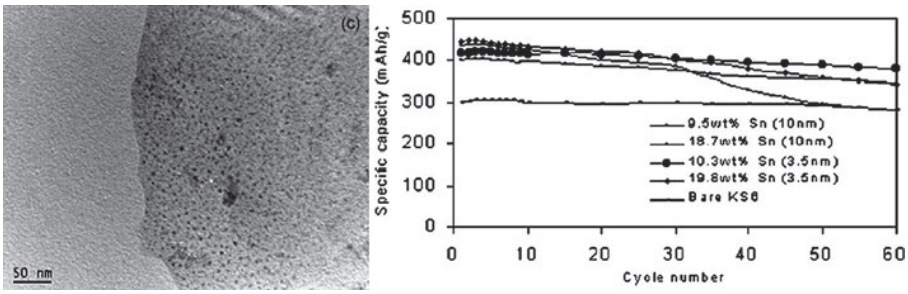

Fig. 25 TEM image of an Sn nanoparticle-loaded graphite and cycling performance of the Sn/C composite. Reproduced with permission.[95]

ultrasonication. It was discovered that with the smaller 3.5 nm Sn nanoparticles a highly reversible lithium ion storage capacity of 415 mAh g^{-1} was attainable with 10.3 wt% loading of Sn (Fig. 25).[95]

In-situ reduction of SnO_2 to Sn in a carbon matrix has also been explored. Here carbon mesospheres containing dispersed SnO_2 nanoparticles were formed by the concurrent carbonization of glucose and pyrolysis of $SnCl_4$ *in-situ*.[28,84] High temperature CVD treatment with an extraneously supplied carbon source was then used to improve the graphitization and reduce encapsulated SnO_2 to Sn.[28,84] The Sn nanoparticles formed as such were catalytic towards the formation of CNTs on the carbon sphere surface.[96,97] The low melting (232 °C) Sn was liquefied under reaction conditions and was siphoned into the interior of the CNTs forming an intriguing hair-like Sn@C core shell structure on the carbon sphere (which looks like the tropical fruit Rambutan) (Fig. 26).[84]

A closer examination revealed the hierarchical structure of the Sn@C composite consisting of tin-containing carbon mesospheres, carbon nanotubes with completely-filled or partially-filled metallic tin interiors, and carbon encapsulated tin nanospheres (Fig. 26). The formation of the hair-like structure in the Rambutan architecture was rationalized by a modified "base growth" mechanism. The unique Sn@C structure could restrain aggregation of nanosized metallic Sn and the presence of 1-D carbon nanotube "hair-like" structures could enhance electrical connectivity and improve the electrical integration of the active materials. The improved electrochemical performance of tin in the nanocomposite could be attributed to this unique morphology.[84]

The template-assisted technique (hard and soft) can be combined with the carbon thermal reduction reaction to fabricate Sn@C nanocomposites.[93,94] This is shown in Fig. 27 using a hard template.[93] In this method, SiO_2 spheres were used to template the formation of SnO_2 hollow spheres first. A thin layer of carbon was then deposited on the surface of the SnO_2 hollow spheres by the carbonization of glucose under hydrothermal conditions. Subsequent calcination of dual-layer SnO_2@C hollow spheres in N_2 reduced SnO_2 to Sn forming an interesting structure of encapsulated Sn nanoparticles in hollow carbon spheres (Fig. 28a) with 74 wt% of Sn loading.[93] Since the hollow carbon spheres provide space for volume excursion during Li_xSn alloying and de-alloying reactions, the Sn@C composite showed high capacity of over 800 mAh g^{-1} for the first 10 cycles, and a high capacity 550 mAh g^{-1} after 100 cycles.[94] Similar morphology could also be created with a soft template.[94] Instead of using SiO_2 as the template, micelles of cetyltrimethylammonium bromide (CTAB) were used as the soft template to form resorcinol formaldehyde (RF) spheres loaded with a Sn precursor (tributylphenyltin). Subsequent *in-situ*

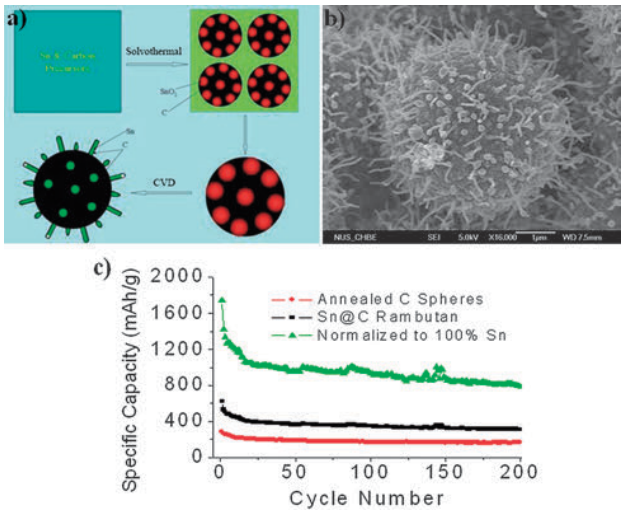

Fig. 26 A schematic (a) shows the steps in the preparation of the Rambutan-like Sn@C composite and (b) an FESEM image of a typical nanostructure. Specific capacity *vs.* cycle number plots of the Rambutan-like Sn@C composite and annealed carbon spheres (c). Reproduced with permission.[84]

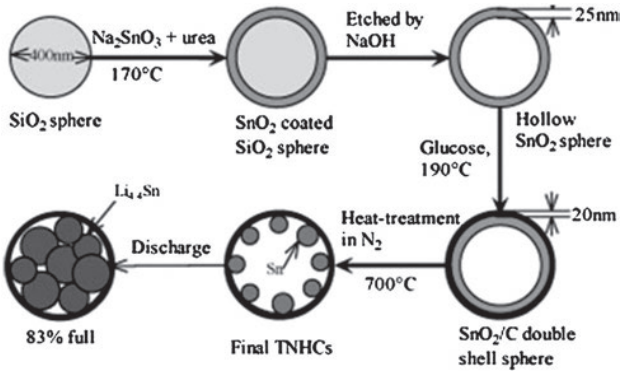

Fig. 27 The fabrication of Sn nanoparticles encapsulated in hollow carbon spheres showing the morphology evolution. Reproduced with permission.[93]

Samsung Ex. 1040, Page 16 of 20
Samsung Electronics Co., Ltd., et al. v. Molecular Rebar Design, LLC
IPR2025-00356

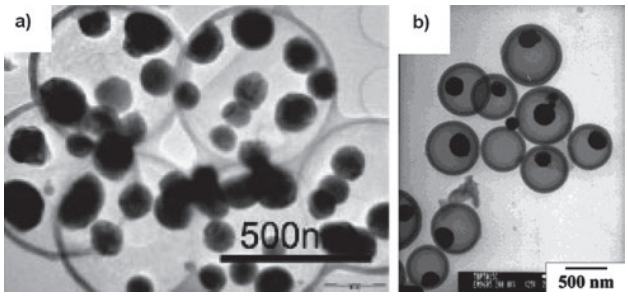

Fig. 28 TEM images of Sn nanoparticles encapsulated in hollow carbon spheres obtained by (a) hard and (b) soft template-assisted methods. Reproduced with permission.[93,94]

calcination carbonized the RF polymer and formed Sn nanoparticles encapsulated in the hollow carbon spheres (Fig. 28b) with 24 wt% Sn.[94]

Although the preparation of Sn/C composites has shown a high level of originality and sophistication in recent years, there are still notable problems of large first cycle irreversible capacity loss and capacity fading in the products.[84,88,94] It is known that for phase-pure Sn, the cycling behavior is inversely proportional to particle size, with sub-4 nm considered to be the most desirable.[88,90] The simple Sn/C composites synthesized so far are limited in their ability to support a high mass loading of small (*i.e.* <4 nm) Sn nanoparticles. The *in-situ* formed Sn nanoparticles by high temperature carbon thermal reduction reaction are much larger in size, ranging from a few tens to a few hundreds of nanometers, and with poor graphitization degrees. Even if the Sn nanoparticles could be made sufficiently small initially, subsequent cycling often leads to aggregation into larger Sn particles, which is the bane of capacity fading. Hence the problems of stabilization of Sn nanoparticles in the carbon matrix and preservation of an electrically integrated network have still to be solved.

3.7. Sn–M/C composite nanostructured anode materials

A new strategy that has drawn increasing attention as a cyclability improvement measure has been to introduce Sn as a Sn M alloy (where M is Sb, Co, Fe, *etc*) into a carbon matrix. For an intermetallic Sn M compound, lithiation of the Sn phase to form a $Li_{x<4.4}Sn$ series of compounds would release the metal M to the surrounding environment. An uniform distribution of the electrically conducting M nanoparticles in close proximity to the Sn storage compound could contribute to the sustenance of electrical integration in the anode. At the same time M could also function as an inactive matrix to inhibit aggregation and size increase the Sn phase. While this concept was mooted some years ago,[87] it is receiving renewed and increased interest after Sony's recent announcement of new generation LIBs based on Sn Co C anode material.[20–23,98] The Sn M/C composites are generally prepared by high energy ball milling.[21] Non-conventional approaches such as the formation of Sn Sb@CNT by *in-situ* CVD,[99] and Sn Ge@C by thermal annealing of butyl-capped $Sn_{78}Ge_{22}$ clusters in vacuum[100] are more recent developments. These techniques could potentially lead to easier production of Sn M/C nanostructures.

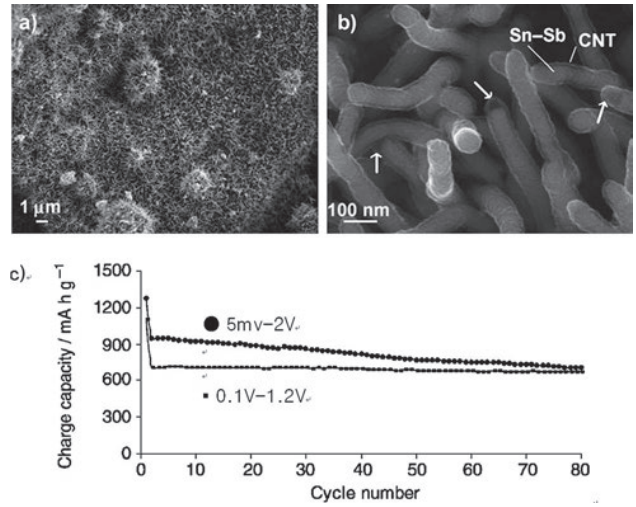

Fig. 29 FESEM images of the carbon nanotube encapsulated Sn–Sb nanorods at (a) low and (b) high magnifications and (c) corresponding cycling performance tested in different voltage windows. Reproduced with permission.[99]

In this first example, commercial antimony tin oxide nanoparticles were processed under CVD conditions at 700 °C using acetylene as the carbon source. Acetylene was able to reduce the metal oxide into intermetallic compounds which then catalyzed the growth of CNTs by C_2H_2 decomposition. At the same time, capillary forces drew the molten intermetallic into the CNT interior, forming CNT-encapsulated Sn Sb nanorods (Fig. 29a,b).[99] When tested for reversible lithium ion storage, these CNT-encapsulated Sn Sb nanorods displayed very high specific capacities and good cyclability (Fig. 29c).[99] The good electrochemical performance could be attributed to the presence of Sb in a lithium-active Sn phase, CNT-enhanced electrical connectivity and the mechanical integrity of the Sn Sb nanorods.

In the second example, branched Sn Ge@C core shell nanowires were prepared by the thermal annealing of butyl-capped $Sn_{78}Ge_{22}$ nanoparticles in vacuum (Fig. 30).[100] The resulting one-dimensional composite materials (50 100 nm in diameter and several micrometers in length) displayed an exceptionally high rate capability (93% coulombic efficiency at 8 C rate) as well as excellent capacity retention after prolonged cycling (94% capacity retention after 45 cycles) (Fig. 30). This impressive electrochemical performance was attributed to the morphology and the presence of the carbon shell which suppressed aggregation into larger particles. In fact the 1-D composite nanowires were found to fragment into smaller nanoparticles and nanowires upon cycling instead of aggregating into larger particles as is typical of metallic Sn.[47]

There are recent reports of Sn Si/C anode materials displaying impressively high capacity (2050 mAh g^{-1}) and good capacity retention (97% after 60 cycles).[101] Other types of Sn-based anode materials with improved electrochemical performance have also been reported, for example tin phosphate,[25,99] SnO_2 filled mesoporous tin phosphate,[102] teardrop-shaped $SnP_{0.94}$[103] and $AlPO_4$ coated SnO_2.[104] Hence there are limitless possibilities for finding a carbon-substitute for the anode; the question is to balance the benefits with mutually compensating features and newly found challenges in scalable production.

This journal is © The Royal Society of Chemistry 2009

Samsung Ex. 1040, Page 17 of 20
Samsung Electronics Co., Ltd., et al. v. Molecular Rebar Design, LLC
IPR2025-00356

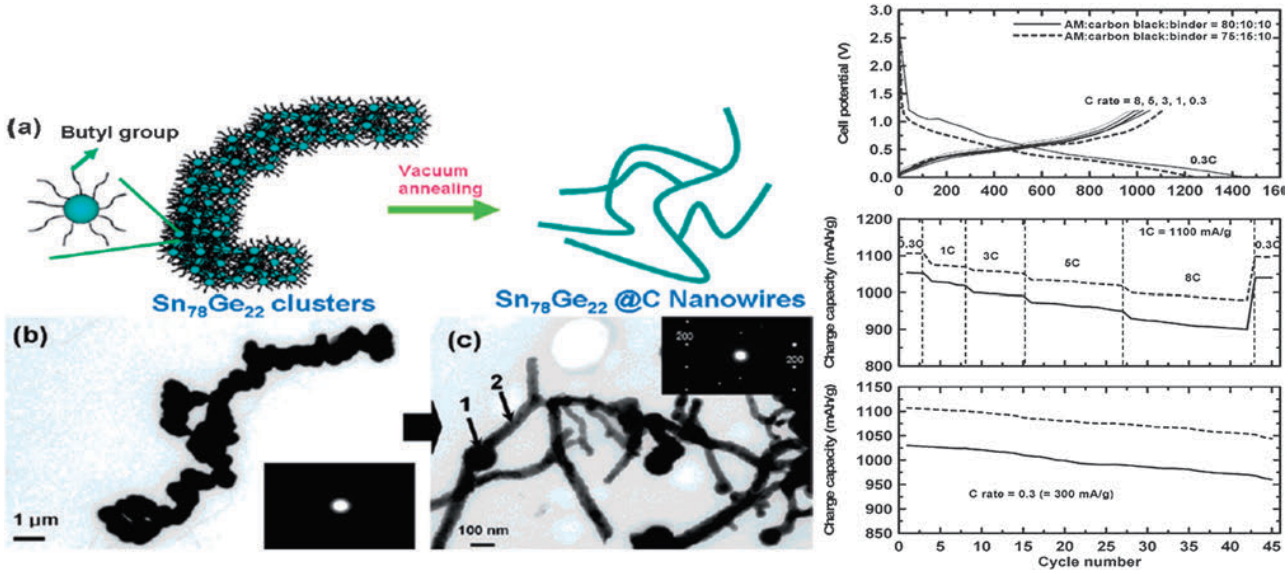

Fig. 30 The formation of $Sn_{78}Ge_{22}$@C nanowires after thermal annealing of the butyl-capped $Sn_{78}Ge_{22}$ nanoparticles clusters in vacuum (left). The electrochemical performance of the $Sn_{78}Ge_{22}$@C nanowires. Reproduced with permission.[100]

4. Conclusion and outlook

Nanostructuring an otherwise mundane material such as TiO_2 and SnO_2 could lead to significant improvements in material performance for reversible Li ion storage. High polarization of bulk TiO_2 is believed to result from slow ionic and electronic diffusion in the active material or interfaces, but manipulation of morphology into nanotubes, nanowires or the control of particle size offer versatile strategies toward improving electrochemical properties. Better rate capabilities that are due to the distance over which Li^+ and electrons must diffuse in the solid state is dramatically decreased in the nanostructured electrode. Furthermore, the high surface area of the nanostructured TiO_2 electrode makes the current density more effective than that of a conventional bulk electrode. Moreover, uniform metallic Sn metals coated onto TiO_2 nanotubes overcome the power density of the TiO_2 electrode material. A thin Sn coating layer is anticipated to facilitate fast and stable Li-ion pathways and allow a smaller amount of conducting-additive carbon to be used to obtain the desired electrochemical performance. An Sn-coated TiO_2 nanotube with low carbon black content can be investigated from the viewpoint of improvement to the volumetric density at a high current rate, 4000 mA g^{-1}, compared to that of bare TiO_2 nanotubes.

Many methods of preparation of SnO_2 including some which are remarkably scalable, cost-effective and environment friendly have been reported to date. Some of them are more attuned to sculpturing complex architecture and hierarchal structures. Many of the methods rely on the use of templates whether extraneously supplied or synthesized *in-situ*. In this regard the preparation of hollow core shell mesospheres of SnO_2 nanoparticle aggregates is of particular interest because templating carbon mesospheres are formed *in-situ* by glucose carbonization and removal of the template; instead of being the usually destructive process, it assisted the formation of the nanostructure in this case. Nevertheless there are indications that the application problem of Sn could not be completely resolved by a phase-pure Sn-based anode. Studies on Sn/C composite anode materials are receiving renewed and boosted interest after Sony' recent announcement of a new LIB series based on the Sn Co C anode. Nanostructuring of more complex Sn M C compounds could be a rewarding undertaking leading to the long-awaited breakthrough in utilizing Li M alloying and dealloying reactions for reversible storage of Li in Sn.

Overall, cell voltage will depend on the choice of the cathode material. If one uses recently introduced 'green' and low-cost $LiFePO_4$ as the cathode (3.4 V *vs.* Li^+/Li), the full cell voltage will be 1.6 V for an anatase TiO_2 anode (~1.8 V *vs.* Li^+/Li) and 2.9 V for a SnO_2 anode (~0.5 V *vs.* Li^+/Li) respectively. For nanostructured TiO_2 anodes, the low full-cell voltage would make the electrodes less reactive towards the electrolyte, resulting in higher electrochemical stability. The freedom from SEI formation on the anode means that Li-ions from the cathode may be used more reversibility without significant first cycle losses. Compared to carbon-based anodes, there will also be less concern for lithium metal deposition, and safety of the full cell is improved as a result. Cyclability is also good. On the other hand, the low cell voltage does result in lower energy density. For Sn-based anodes, although the full-cell voltage will be higher in this case, it will be not as flat because of the lack of extended voltage plateaus in the charge/discharge profiles. The larger changes in the electrode volume during charge/discharge also result in poorer electrochemical stability. Sn-based anode materials are also beset by significant first cycle irreversible capacity losses due to poor SEI quality which consume more Li ions from the cathode.

Acknowledgements

This work was supported by the IT R&D program of MKE/IITA (Core Lithium Secondary Battery Anode Materials for Next Generation Mobile Power Module, 2008-F-019-01). XAS experiments were carried out at Pohang Light Source (PLS).

Samsung Ex. 1040, Page 18 of 20
Samsung Electronics Co., Ltd., et al. v. Molecular Rebar Design, LLC
IPR2025-00356

Support from the WCU (world class university) program (MEST) is greatly acknowledged.

References

1 P. G. Bruce, B. Scrosti and J.-M. Tarascon, *Angew. Chem., Int. Ed.*, 2008, **47**, 2930.
2 M. Winter and R. J. Brodd, *Chem. Rev.*, 2004, **104**, 4245.
3 M. Winter, J. O. Besenhard, M. E. Spahr and P. Novak, *Adv. Mater.*, 1998, **10**, 725.
4 X. Chen and S. S. Mao, *Chem. Rev.*, 2007, **107**, 2891.
5 T. Kasuga, M. Hiramatsu, A. Hoson, T. Sekino and K. Niihara, *Langmuir*, 1998, **14**, 3160.
6 T. Kasuga, M. Hiramatsu, A. Hoson, T. Sekino and K. Niihara, *Adv. Mater.*, 1999, **11**, 1307.
7 J. H. Pan, X. Zhang, A. J. Du, D. D. Sun and J. O. Leckie, *J. Am. Chem. Soc.*, 2008, **130**, 11256.
8 G. R. Patzke, F. Krumeich and R. Nesper, *Angew. Chem., Int. Ed.*, 2002, **41**, 2446.
9 H. Yin, Y. Wada, T. Kitamura, S. Kambe, S. Murasawa, H. Mori, T. Sakata and S. Yanagida, *J. Mater. Chem.*, 2001, **11**, 1694.
10 Q. Chen, W. Zhou, G. Du and L.-M. Peng, *Adv. Mater.*, 2002, **14**, 1208.
11 L. Kavan, M. Kalbáč, M. Zukalová, I. Exnar, V. Lorenzen, R. Nesper and M. Graetzel, *Chem. Mater.*, 2004, **16**, 477.
12 H. Zhang, G. R. Li, L. P. An, T. Y. Yan, X. P. Gao and H. Y. Zhu, *J. Phys. Chem. C*, 2007, **111**, 6143.
13 A. S. Arico, P. Bruce, B. Scrosati, J. M. Tarascon and W. Van Schalkwijk, *Nat. Mater.*, 2005, **4**, 366.
14 J. M. Tarascon and M. Armand, *Nature*, 2001, **414**, 359.
15 K. T. Nam, D. W. Kim, P. J. Yoo, C. Y. Chiang, N. Meethong, P. T. Hammond, Y. M. Chiang and A. M. Belcher, *Science*, 2006, **312**, 885.
16 L. Taberna, S. Mitra, P. Poizot, P. Simon and J. M. Tarascon, *Nat. Mater.*, 2006, **5**, 567.
17 Nippon Denki Shinbun, 1996, March 11, www.shinbun.denki.or.jp/english.
18 Y. Idota, T. Kubota, A. Matsufuji, Y. Maekawa and T. Miyasaka, *Science*, 1997, **276**, 1395.
19 P. Poizot, S. Laruelle, S. Grugeon, L. Dupont and J. M. Tarascon, *Nature*, 2000, **407**, 496.
20 H. Inoue, *International Meeting on Lithium Batteries: Abstr. #228*, 2006, Biarritz, France.
21 J. Hassoun, G. Mulas, S. Panero and B. Scrosati, *Electrochem. Commun.*, 2007, **9**, 2075.
22 A. D. W. Todd, R. A. Dunlap and J. R. Dahn, *J. Alloys Compd.*, 2007, **443**, 114.
23 J. R. Dahn, R. E. Mar and A. Abouzeid, *J. Electrochem. Soc.*, 2006, **153**, A361.
24 N. C. Li, C. R. Martin and B. Scrosati, *Electrochem. Solid-State Lett.*, 2000, **3**, 316.
25 E. Kim, D. Son, T. G. Kim, J. Cho, B. Park, K. S. Ryu and S. H. Chang, *Angew. Chem., Int. Ed.*, 2004, **43**, 5987.
26 D. Deng and J. Y. Lee, *Chem. Mater.*, 2007, **19**, 4198.
27 P. G. Bruce, B. Scrosati and J. M. Tarascon, *Angew. Chem., Int. Ed.*, 2008, **47**, 2930.
28 D. Deng and J. Y. Lee, *Chem. Mater.*, 2008, **20**, 1841.
29 M. V. Koudriachova, N. M. Harrison and S. W. Leeuw, *Solid State Ionics*, 2003, **157**, 35.
30 M. C. Payne, M. P. Teter, D. C. Allan, T. A. Arias and J. D. Joannapulos, *Rev. Mod. Phys.*, 1992, **64**, 1045.
31 M. V. Koudriachova, N. M. Harrison and S. W. Leeuw, *Phys. Rev. B: Condens. Matter Mater. Phys.*, 2002, **65**, 235423.
32 A. Stashans, S. Lunell and R. Bergstroem, *Phys. Rev. B*, 1996, **53**, 159.
33 M. V. Koudriachova, N. M. Harrison and S. W. Leeuw, *Phys. Rev. Lett.*, 2001, **86**, 1275.
34 W. J. Macklin and R. J. Neat, *Solid State Ionics*, 2003, **157**, 35.
35 Y.-S. Hu, L. Kienle, Y.-G. Guo and J. Maier, *Adv. Mater.*, 2006, **18**, 1421.
36 W. J. H. Borghols, M. Wagemaker, U. Lafont, E. M. Kelder and F. M. Mulder, *Chem. Mater.*, 2008, **20**, 2949.
37 M. Wagemaker, W. J. H. Borghols and F. M. Mulder, *J. Am. Chem. Soc.*, 2007, **129**, 4323.
38 C. Jiang, I. Honma, T. Kudo and H. Zhou, *Electrochem. Solid-State Lett.*, 2007, **10**, A127.
39 G. Nuspl, K. Yoshizawa and T. Yamabe, *J. Mater. Chem.*, 1997, **7**, 2529.
40 M. Wagemaker, R. Krol, A. P. M. Kentgens, A. A. Well and F. M. Mulder, *J. Am. Chem. Soc.*, 2001, **123**, 111454.
41 T. Ohzuku, T. Kodama and T. Hirai, *J. Power Sources*, 1985, **14**, 153.
42 D. W. Murphy, M. Greenblatt, S. M. Zahurak, R. J. Cava, J. V. Waszczak, G. W. Hull and R. S. Hutton, *Rev. Chim. Miner.*, 1982, **19**, 441.
43 G. Sudant, E. Baudrin, D. Larcher and J.-M. Tarascon, *J. Mater. Chem.*, 2005, **15**, 1263.
44 S.-J. Bao, Q.-L. Bao, C.-M. Li and Z.-L. Dong, *Electrochem. Commun.*, 2007, **9**, 1233.
45 H. G. Yang and H. C. Zeng, *J. Phys. Chem. B*, 2004, **108**, 3492.
46 J. Li, Z. Tang and Z. Zhang, *Electrochem. Solid-State Lett.*, 2005, **8**, A316.
47 S.-H. Kang, J. B. Goodenough and L. K. Rabenberg, *Electrochem. Solid-State Lett.*, 2001, **4**, A49.
48 M. Wei, Y. Konishi, H. Zhou, H. Sugihara and H. Arakawa, *Solid State Commun.*, 2005, **133**, 493.
49 D. V. Bavykin, J. M. Friedrich and F. C. Walsh, *Adv. Mater. (Weinheim, Ger.)*, 2006, **18**, 1.
50 Q. Chen, G. H. Du, S. Zhang and L.-M. Peng, *Acta Crystallogr., Sect. B: Struct. Sci.*, 2002, **B58**, 587.
51 T. P. Feist and P. K. Davies, *J. Solid State Chem.*, 1992, **101**, 275.
52 X. Sun and Y. Li, *Chem.–Eur. J.*, 2003, **9**, 2229.
53 J.-N. Nian and H. Teng, *J. Phys. Chem. B*, 2006, **110**, 4193.
54 Q. Wang, Z. Wen and J. Li, *Inorg. Chem.*, 2006, **45**, 6944.
55 X. P. Gao, Y. Lan, H. Y. Zhu, J. W. Liu, Y. P. Ge, F. Wu and D. Y. Song, *Electrochem. Solid-State Lett.*, 2005, **8**, A26.
56 C. Jiang, M. Wei, Z. Qi, T. Kudo, I. Honma and H. Zhou, *J. Power Sources*, 2007, **166**, 239.
57 B. Song, S. Liu, J. Jian, M. Lei, X. Wang, H. Li, J. Yu and X. Chen, *J. Power Sources*, 2008, **180**, 869.
58 J. Xu, C. Jia, B. Cao and W. F. Zhang, *Electrochim. Acta*, 2007, **52**, 8044.
59 Y. Lan, X. Gao, H. Zhu, Z. Zheng, T. Yan, F. Wu, S. P. Ringer and D. Song, *Adv. Funct. Mater.*, 2005, **15**, 1310.
60 Y.-G. Guo, Y.-S. Hu and J. Maier, *Chem. Commun.*, 2006, 2783.
61 G. Armstrong, A. R. Armstrong, J. Canales and P. G. Bruce, *Electrochem. Solid-State Lett.*, 2006, **9**, A139.
62 A. R. Armstrong, G. Armstrong, J. Canales and P. G. Bruce, *Angew. Chem., Int. Ed.*, 2004, **43**, 2286.
63 A. R. Armstrong, G. Armstrong, J. Canales and P. G. Bruce, *Adv. Mater.*, 2005, **17**, 862.
64 I. Moriguchi, R. Hidaka, H. Yamada, T. Kudo, H. Murakami and N. Nakashima, *Adv. Mater.*, 2006, **18**, 69.
65 Y.-G. Guo, Y.-S. Hu, W. Sigle and J. Maier, *Adv. Mater.*, 2007, **19**, 2087.
66 (*a*) H. Kim, M. G. Kim, T. J. Shin, H.-J. Shin and J. Cho, *Electrochem. Commun.*, 2008, **10**, 1669; (*b*) unpublished work.
67 S. O. Kucheyev, T. van Buuren, T. F. Baumann, J. H. Satcher, T. M. Willey, R. W. Meulenberg, T. E. Felter and J. Terminello, *J. Phys. Rev. B*, 2004, **69**, 245102.
68 J. Kim and J. Cho, *Electrochem. Solid-State Lett.*, 2007, **10**, A81.
69 X. W. Lou, C. L. Yuan and L. A. Archer, *Adv. Mater.*, 2007, **19**, 3328.
70 Y. Wang, H. C. Zeng and J. Y. Lee, *Adv. Mater.*, 2006, **18**, 645.
71 Y. Wang, F. B. Su, J. Y. Lee and X. S. Zhao, *Chem. Mater.*, 2006, **18**, 1347.
72 X. W. Lou, Y. Wang, C. L. Yuan, J. Y. Lee and L. A. Archer, *Adv. Mater.*, 2006, **18**, 2325.
73 Y. Wang, J. Y. Lee and H. C. Zeng, *Chem. Mater.*, 2005, **17**, 3899.
74 Y. Wang, J. Y. Lee and T. C. Deivaraj, *J. Phys. Chem. B*, 2004, **108**, 13589.
75 H. Kim and J. Cho, *J. Mater. Chem.*, 2008, **18**, 771.
76 Y. Wang and J. Y. Lee, *J. Phys. Chem. B*, 2004, **108**, 17832.
77 Y. Yu, C. H. Chen and Y. Shi, *Adv. Mater.*, 2007, **19**, 993.
78 C. Kim, M. Noh, M. Choi, J. Cho and B. Park, *Chem. Mater.*, 2005, **17**, 3297.
79 Y. Wang and J. Y. Lee, *J. Power Sources*, 2005, **144**, 220.
80 J. Y. Lee, R. F. Zhang and Z. L. Liu, *Electrochem. Solid-State Lett.*, 2000, **3**, 167.

This journal is © The Royal Society of Chemistry 2009

Samsung Ex. 1040, Page 19 of 20
Samsung Electronics Co., Ltd., et al. v. Molecular Rebar Design, LLC
IPR2025-00356

81 J. Fan, T. Wang, C. Z. Yu, B. Tu, Z. Y. Jiang and D. Y. Zhao, *Adv. Mater.*, 2004, **16**, 1432.
82 H. Qiao, Z. Zheng, L. Z. Zhang and L. F. Xiao, *J. Mater. Sci.*, 2008, **43**, 2778.
83 T. Moon, C. Kim, S. T. Hwang and B. Park, *Electrochem. Solid-State Lett.*, 2006, **9**, A408.
84 D. Deng and J. Y. Lee, *Angew. Chem., Int. Ed.*, 2009, **48**, 1660.
85 J. Hassoun, G. Derrien, S. Panero and B. Scrosati, *Adv. Mater.*, 2008, **20**, 3169.
86 G. Derrien, J. Hassoun, S. Panero and B. Scrosati, *Adv. Mater.*, 2007, **19**, 2336.
87 M. Winter and J. O. Besenhard, *Electrochim. Acta*, 1999, **45**, 31.
88 W. M. Zhang, J. S. Hu, Y. G. Guo, S. F. Zheng, L. S. Zhong, W. G. Song and L. J. Wan, *Adv. Mater.*, 2008, **20**, 1160.
89 K. T. Lee, Y. S. Jung and S. M. Oh, *J. Am. Chem. Soc.*, 2003, **125**, 5652.
90 Y. Wang, J. Y. Lee and T. C. Deivaraj, *J. Electrochem. Soc.*, 2004, **151**, A1804.
91 M. Noh, Y. Kwon, H. Lee, J. Cho, Y. Kim and M. G. Kim, *Chem. Mater.*, 2005, **17**, 1926.
92 M. Noh, Y. Kim, M. G. Kim, H. Lee, H. Kim, Y. Kwon, Y. Lee and J. Cho, *Chem. Mater.*, 2005, **17**, 3320.
93 W. M. Zhang, J. S. Hu, Y. G. Guo, S. F. Zheng, L. S. Zhong, W. G. Song and L. J. Wan, *Adv. Mater.*, 2008, **20**, 1160.
94 K. T. Lee, Y. S. Jung and S. M. Oh, *J. Am. Chem. Soc.*, 2003, **125**, 5652.
95 Y. Wang, J. Y. Lee and T. C. Deivaraj, *J. Electrochem. Soc.*, 2004, **151**, A1804.
96 R. Y. Li, X. C. Sun, X. R. Zhou, M. Cai and X. L. Sun, *J. Phys. Chem. C*, 2007, **111**, 9130.
97 L. Jankovic, D. Gournis, P. N. Trikalitis, I. Arfaoui, T. Cren, P. Rudolf, M. H. Sage, T. T. M. Palstra, B. Kooi, J. De Hosson, M. A. Karakassides, K. Dimos, A. Moukarika and T. Bakas, *Nano Lett.*, 2006, **6**, 1131.
98 H. Kim and J. Cho, *Electrochim. Acta*, 2007, **52**, 4197.
99 Y. Wang and J. Y. Lee, *Angew. Chem., Int. Ed.*, 2006, **45**, 7039.
100 H. Lee and J. Cho, *Nano Lett.*, 2007, **7**, 2638.
101 Y. Kwon and J. Cho, *Chem. Commun.*, 2008, 1109.
102 J. Y. Kim and J. Cho, *Electrochem. Solid-State Lett.*, 2006, **9**, A373.
103 Y. Kim, H. Hwang, C. S. Yoon, M. G. Kim and J. Cho, *Adv. Mater.*, 2007, **19**, 92.
104 T. J. Kim, D. Son, J. Cho, B. Park and H. Yang, *Electrochim. Acta*, 2004, **49**, 4405.

This journal is © The Royal Society of Chemistry 2009

Samsung Ex. 1040, Page 20 of 20
Samsung Electronics Co., Ltd., et al. v. Molecular Rebar Design, LLC
IPR2025-00356